Vibration transmission through the seated human body captured with a computationally efficient multibody model

Desai, Raj; Papaioannou, Georgios; Happee, Riender

DOI
10.1007/s11044-024-10025-1

Publication date
2024

Document Version
Final published version

Published in
Multibody System Dynamics

Multibody System Dynamics
https://doi.org/10.1007/s11044-024-10025-1

RESEARCH

Vibration transmission through the seated human body captured with a computationally efficient multibody model

Raj Desai[1,2] · **Georgios Papaioannou**[1] · **Riender Happee**[1]

Received: 27 December 2023 / Accepted: 9 August 2024

Abstract

Existing models of vibration transmission through the seated human body are primarily two-dimensional, focusing on the mid-sagittal plane and in-plane excitation. However, these models have limitations when the human body is subjected to vibrations in the mid-coronal plane. Three-dimensional (3D) human models have been primarily developed for impact analysis. Recently, we showed that such a 3D active human model can also predict vibration transmission. However, existing 3D body models suffer from excessive computational time requirements due to their complexity. To effectively analyze motion comfort, this research presents a 3D computationally efficient human model (EHM), running faster than real-time, with scope for real-time vehicle and seat motion control to enhance comfort. The EHM is developed by considering various combinations of body segments and joint degrees of freedom, interacting with multibody (MB) and finite element (FE) seat compliance models. Postural stabilization parameters are estimated using an optimization process based on experimental frequency-dependent gain responses for different postures (erect/slouched) and backrest support (low/high) conditions. The model combines two postural control mechanisms: 1) joint angle control capturing reflexive and intrinsic stabilization for each degree of freedom with PID controllers, including integration to eliminate drift, and 2) head-in-space control minimizing 3D head rotation. Interaction with a compliant seat was modeled using deformable finite elements and multibody contact models. Results showed the importance of modeling both compressive and shear deformation of the seat and the human body. Traditional stick-slip multibody contact failed to reproduce seat-to-human vibration transmission. Combining efficient body modeling principles, innovative postural adaptation techniques, and advanced seat contact strategies, this study lays a robust foundation for predicting and optimizing motion comfort.

Keywords Multibody · Vibration · Comfort · Postural stabilization · Automated driving · Seat design

✉ R. Desai
r.r.desai@tudelft.nl; ae4514@coventry.ac.uk

1 Intelligent Vehicles Group, Cognitive Robotics, Delft University of Technology, Delft, The Netherlands

2 Present address: Centre for Future Transport and Cities, Coventry University, Coventry, UK

Published online: 06 September 2024

1 Introduction

Automated driving (AD) holds great promise in providing safe and sustainable transport. Automation will allow users to take their eyes off the road, freeing up time for work or leisure activities. This will require high comfort levels [1] achieved by smooth driving styles and innovative interiors. A particular concern in AD is car sickness, from which two-thirds of passengers suffer during eye off-road conditions, which could include engagement in non-driving activities like reading or using digital devices. Such conditions might affect occupants' overall postural stability. Being exposed to whole-body vibration (WBV) produced by the vehicle, occupants may feel discomfort, while such vibrations could even cause low back pain and injuries in the lumbar spine [2–5]. Hence, knowledge and models of human postural stabilization and motion perception are essentially needed for the human-centered design of automated driving systems. Therefore, it is crucial to investigate how vibrations are transmitted through the human body and how they affect motion discomfort while driving in automated vehicles [6]. Even if using experimental data to understand human motion and comfort is an effective method [7], it costs human resources and could cause health discomfort to the participants. Meanwhile, conducting extensive experiments capturing relevant on-road conditions is not realistic. Thus, the need for a computationally efficient and accurate 3D human body model to predict human responses to diverse motion stimuli has risen, and this is where this work will focus.

Generally, biomechanical human body models are categorized into three categories: lumped mass models [8–10], multibody models [11–15], and finite element (FE) models [16–21]. Lumped mass models are the simplest in which human body segments are regarded as rigid mass and can only have translational movement in one direction. Finite Element (FE) models consist of large numbers of mass, spring solid, and beam elements and are mostly used to model detailed structures (i.e., skeletons, muscles, and body kinematics). However, due to the high complexity, FE computations are time-consuming, and multibody human body models are a viable alternative. Multibody human body models [22] require overall dimensions and inertia of each human body segment and allow translational and rotational joint movements in 3D. The consideration of more degrees of freedom (DoF) could secure a better representation than the lumped mass models; however, this will increase the number of model parameters.

Madymo [23] (MAthematical DYnamic MOdel) is an advanced software that simulates the dynamic behavior of physical systems, emphasizing the analysis of vehicle collisions and assessing injuries sustained by passengers. Madymo provides a range of validated human body models, mainly using multibody techniques [24–28]. The main difference between the human model types lies in the modeling techniques applied to represent the surface geometry. The most computationally efficient models use ellipsoids, whereas more advanced models use 3D undeformable FE surfaces, also referred to as facet surfaces [27]. Both ellipsoid and facet surfaces can interact with other surfaces using nonlinear stiffness and damping functions, as well as deformable FE structures.

The Madymo Active Human Model (AHM) was originally developed for injury assessment in road accidents [25–27, 29–32] and was recently shown to also be suitable to simulate comfort-related body motion in vibration and dynamic driving [33]. However, the AHM is computationally demanding due to a large number of degrees of freedom, including all vertebral bodies and allowing 6DOF motion (3DOF rotation and 3DOF translation) in all intervertebral joints, the detailed joint structure models and postural stabilization using nonlinear Hill-type line-element muscle models. The AHM body surface is described using facets, enhancing realism when interacting with seats but increasing the computational demand for contact interactions. Such detail may be relevant and acceptable for high-severity

crash simulations where actual events are generally shorter than half a second. However, such specifics may not be needed for vibration and general comfort studies, including motion sickness, where driving experiments and simulations with durations like 30 minutes are common, and for in-vehicle applications where real-time operation is needed.

Due to the complexity and computational cost, there is an increasing demand for more efficient human body models. Models confined to two dimensions struggle to fully capture the complexities of human body dynamics, especially in scenarios involving vibration and impact. Vibration transmitted through the seat can occur in multiple planes [34], including sagittal, coronal, and transverse [35]. 2D models, being confined to a single plane, cannot fully capture the interaction between different body segments and the resulting dynamic responses. Human seat interaction involves complex interactions between various body segments in three-dimensional space [36]. A 3D full-body model allows for a more comprehensive representation of these interactions, enabling a more accurate simulation of occupant dynamics. Hence, the objective of this paper is to develop and validate an efficient multibody seated human body model that can be used for analyzing human responses in vehicle environments. In this regard, we present a new 3D multibody human model using ellipsoid surfaces, which will be further referred to as the computationally efficient human model (EHM). The deformation of soft tissues (like flesh and skin) is represented by force-based contact characteristics. We validate this model in 3D vibration on a compliant automotive seat using recent experimental data [7]. More specifically, we consider the body's head, trunk, and pelvis 3D motion in translation (x-y-z) and rotation (roll-pitch-yaw) in response to 3D seat vibration. Realistic contacts with the floor, seat base, and back are incorporated to represent seat interactions as a dependent function of posture.

The paper describes the biomechanical model and postural stabilization (Sect. 2), the applied validation data and parameter estimation (Sect. 3), seat compliance models (Sect. 4), followed by accuracy and computational cost for several seat modeling methods for the new EHM model and the existing AHM [37] (Sect. 5), and validation results for three posture and seat back conditions (Sect. 6).

2 Biomechanical model

In order to build an efficient seated human body model, we evaluated a range of published human body models for impact simulation and vibration comfort simulation. In full-body biomechanical models, the complete lumbar, thoracic, and cervical spine is generally modeled, defining all vertebrae as separate rigid bodies [17, 20, 38, 39]. The intervertebral joints are mostly represented by 6 degrees of freedom (DoF) joints, allowing compression, shear, and 3D rotation. The low inertia of the vertebrae and the high stiffness of the intervertebral joints require small timesteps, particularly for the neck [21, 40, 41]. Soft tissues and the rib cage are either lumped into the vertebral inertia or defined as additional deformable structures [12, 42, 43]. Passive joint properties are defined using nonlinear multibody [44] and or FE models, and postural stabilization is realized through controlled line element muscles or controlled joint actuators, applying torques directly. Full-body finite element models are extremely computationally demanding and include relatively simple models of postural stabilization [17, 20, 38]. At this stage, the most suitable reference model is the Madymo Active Human Model (AHM) [37], which includes a full multisegment spine. The AHM uses multibody techniques and is therefore more computationally efficient compared to deformable FE human models. The AHM was initially designed for impact conditions, and we recently showed that it also captures dynamic driving and vibration transmission [33]. Hence, the AHM [37] is used as a reference to validate the newly developed EHM.

2.1 Body segments and anthropometry

For enhanced predictive capabilities while minimizing computational overhead, a strategic reduction of DoFs and stabilizing structures was achieved for the Efficient Human Model (EHM). The entire spine was divided into six bodies connected by five joints (Table 1). This segmentation is similar to models used in ergonomic studies to assess postural comfort [45–47]. Legs and feet are incorporated to realistically simulate how a seated human body responds to vehicle vibration and stabilize the trunk in dynamic driving [33]. The arms are lumped into the upper torso inertia since our research focused on the head/trunk/pelvis. Narrowing our focus to these areas, we were able to provide a more detailed and targeted analysis of vibration transmission dynamics without introducing additional computational burden associated with modeling the arms. However, arms can be added in future models with a level of complexity and postural stabilization adapted to the conditions to be studied [48, 49].

Mid-size male anthropometry (50th percentile) was adopted with size and inertia parameters from published anthropometry measures as a standard representation [50]. While individual variations in anthropometry will influence the results, our approach aimed to capture an average response over a range of participants, yielding a generalized understanding of the vibration transmission phenomena rather than individualizing the model per participant. The anthropometry of the human model included the following main parameter values: standing height of 1.76 meters, erect sitting height of 0.92 meters, and weight of 75.3 kilograms. Moments of inertia were calculated according to the model's shape of each segment (Table 1). In the EHM model, the positioning of the joints and the location of the CG for each segment were critical considerations for the realistic prediction of the dynamics and kinematics [51]. The type of joint and its positioning ensures that the model can accurately simulate the biomechanics of human motion, capturing essential aspects of joint behavior and movement dynamics, while accurate CG locations for each segment help to capture the segmental mass distribution and its effect on overall motion dynamics. The CG of each body part in the EHM was carefully positioned to match the location of the AHM during the initial positioning of the model. In the selected coordinate system, the pelvis serves as the origin, and the locations of the CG of various bodies and joints are expressed relative to the pelvis. The skin is represented by third-order ellipsoids to create a rather smooth and realistic surface. The efficient model is overlaid with the AHM to illustrate the symmetric nature and true anthropometric characteristics of the human body in Fig. 1. In this reference condition, the backrest is inclined at an angle of 12 degrees from the vertical, while the seat pan is inclined at an angle of 5 degrees from the horizontal. Similarly, the footrest is inclined at an angle of 5 degrees from the horizontal.

2.2 Joint degrees of freedom

To enhance computational efficiency, the EHM predominantly employs rotational joints, complemented with one translational joint capturing spinal compression. Figure 2 illustrates all bodies and joints whereas Table 2 summarizes the joint configuration together with the joint coordinates. A spherical joint (J_1) at the upper neck at the C1–C0 intervertebral joint location captures head roll-pitch-yaw and a universal joint (J_2) at the lower neck (T1–C7 joint location) captures roll-pitch motion [52]. Yaw is omitted at the lower neck joint J_2 since neck axial mobility is concentrated in the upper neck and is largest in the atlas-dens joint [53]. The upper torso connects with the middle torso at T12 (J_3), whereas the middle torso connects with the lower torso at L4–L5 (J_4). Both joints allow 3D rotation through spherical

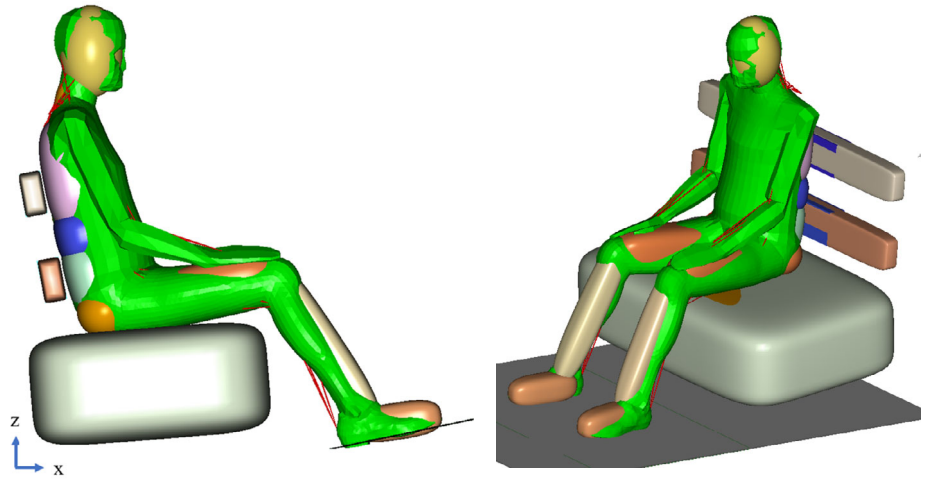

Fig. 1 AHM (green mesh and red muscles) overlaid with EHM (ellipsoids)

Table 1 Body segment data. (The center of gravity is expressed relative to the pelvis)

Body	Ellipsoid Degree	Mass kg	Moments of Inertia (kg·m^2)			Centre of Gravity Coordinates (m)		
			I_{xx}	I_{yy}	I_{zz}	x	y	z
Head	2	6.237	0.018	0.023	0.017	−0.05	0.00	0.69
Neck	2	1.6	0.0035	0.0040	0.0055	−0.09	0.00	0.57
Upper torso with arms	3	13.34	0.355	0.218	0.270	−0.08	0.00	0.35
Middle torso	3	7.7	0.238	0.146	0.181	−0.04	0.00	0.16
Lower torso	3	10.70	0.137	0.078	0.117	0.00	0.00	0.05
Pelvis	2	10.93	0.115	0.050	0.151	0.00	0.00	0.00
Thigh right	3	7.7	0.007	0.129	0.129	0.22	0.11	0.03
Thigh left	3	7.7	0.007	0.129	0.129	0.22	−0.11	0.03
Leg right	3	3.58	0.031	0.031	0.020	0.55	0.15	−0.10
Leg left	3	3.58	0.031	0.031	0.020	0.55	−0.15	−0.10
Foot right	3	1.116	0.001	0.005	0.004	0.75	0.17	−0.31
Foot left	3	1.116	0.001	0.005	0.004	0.75	−0.17	−0.31

joints. A "vertical" translational joint is added at J_3 to capture spinal compression/expansion in a direction aligned with a vector connecting J3 and J4 (see red arrow in Fig. 2). This vertical motion is critical for capturing the entire spinal response in vertical vibration transmission. To combine 3D rotation with 1D translation, we added a virtual body with negligible mass. A translational joint connects the virtual body to the middle torso, while a spherical joint connects it to the upper torso. The spherical joint J_4 is placed at L4–L5, which is shown to approximate the lumbar bending rotation center well in dynamic perturbation experiments in seated participants with their pelvis fixed [54]. Another spherical joint (J_5) connects the pelvis with the lower torso, but this joint is currently locked, as adding mobility in this location did not improve the results. Thus, (J_3-J_4) are used to represent torso

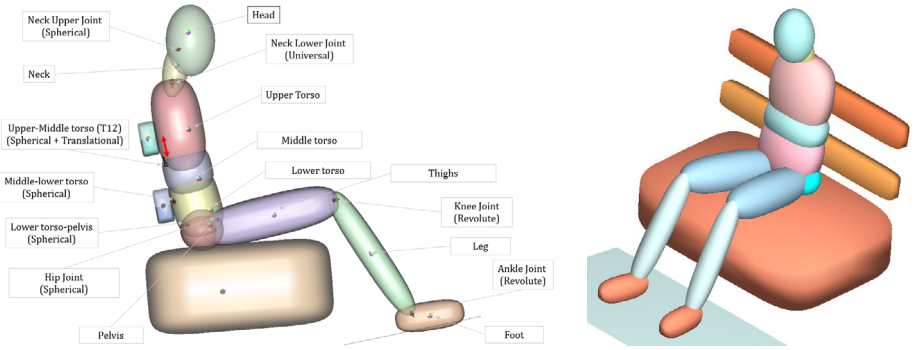

Fig. 2 Computationally Efficient Human Model (EHM) in an erect posture with high backrest

Table 2 Model joint configuration. The red arrow illustrates translation (Trans) in "vertical" direction along a line connecting J3 and J4. Revolute joint axes are oriented perpendicular to the plane formed by the thighs, legs, and feet

Joint	Connected body segments		Joint type	Coordinates (m)		
				x	y	z
Upper Neck (J_1)	Head	Neck	Spherical	−0.09	0.00	0.63
Lower Neck (J_2)	Neck	Upper Torso	Universal	−0.11	0.00	0.51
T12 joint (J_3)	Upper Torso	Middle Torso	Spherical + Trans	−0.16	0.00	0.23
L4–L5 joint (J_4)	Middle Torso	Lower Torso	Spherical	−0.13	0.00	0.08
Sacroiliac joint (J_5)	Lower Torso	Pelvis	Spherical (Locked)	−0.08	0.00	0.00
Hip joint right (J_6)	Pelvis	Thigh right	Spherical	0.03	0.09	0.02
Hip joint left (J_7)	Pelvis	Thigh left	Spherical	0.03	−0.09	0.02
Knee right (J_8)	Thigh right	Leg right	Revolute	0.43	0.14	0.09
Knee left (J_9)	Thigh left	Leg left	Revolute	0.43	−0.14	0.09
Ankle right (J_{10})	Leg right	Foot right	Revolute (Locked)	0.69	0.16	−0.31
Ankle left (J_{11})	Lower leg	Foot left	Revolute (Locked)	0.69	−0.16	−0.31

flexion extension, abduction-adduction, and yaw rotation. The right and left hip joints are represented as spherical joints that connect the two thighs to the pelvis, labeled J_6 and J_7, respectively. Revolute joints are used to simulate the right and left knees, allowing thighs and lower legs to rotate relative to one axis, which are designated by J_8 and J_9, respectively. Ankles are represented as revolute joints that link the lower legs and feet (J_{10} and J_{11}). The ankle joints are locked for simplicity in the present study at an angle adapted to the specific posture. Having ankle joints also allows for activation and modification in future model iterations without necessitating major structural changes.

2.3 Postural stabilization

Postural stabilization models generally include separate models of 1) passive joint resistance, 2) joint "stiffening" achieved via co-contraction of antagonist muscle groups, and 3) dynamic muscular stabilization [55–60]. For the EHM, we have chosen to lump and linearise these three components. To simplify the parameter estimation, linear stiffness and

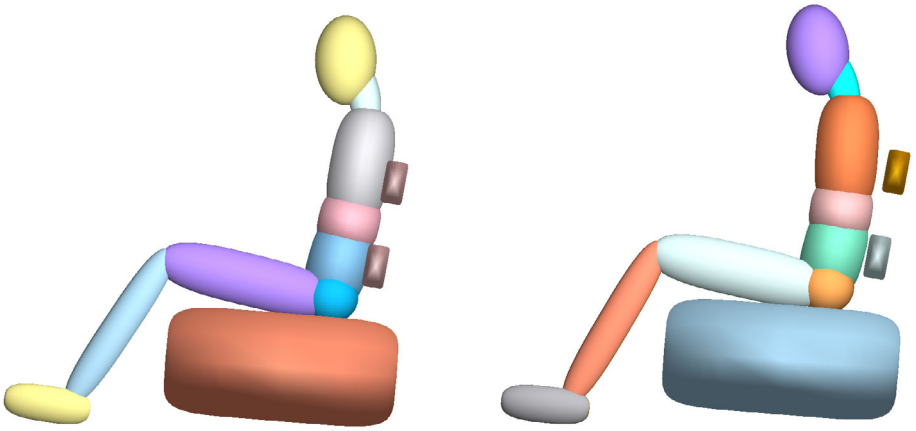

(a) With integrators, the defined posture was maintained.

(b) Without integrators, the defined posture was not maintained.

Fig. 3 Body posture after settling

damping properties are attributed to each joint's degree of freedom. Initially, linear stiffness and damping were implemented using the Cardan restraint concept. This restraint entails the application of three parallel torsional springs and dampers, linking two anatomical segments. The resulting torques depend on Cardan angles, which intricately explain how the related restraint coordinate systems are aligned with one another. However, low stiffness values were found during model fitting, especially in the neck region. Such low stiffness values concur with biomechanical measurements of passive neck bending stiffness at low excursions [61, 62]. Where the AHM and derived models [63] include nonlinear joint properties as needed for impact, we focus on low amplitude vibration, justifying linear joint resistance properties. With both options (linear vs. nonlinear), the neck has a limited bending resistance at low bending angles. In the selected erect posture, the head and trunk centers of gravity are located in front of the joints, stabilizing the trunk and neck. Hence, the actual body posture in prolonged simulations differed from the desired configuration as a result of substantial postural drift (see Fig. 3 left). To overcome this drift, Proportional-Integral-Derivative (PID) controllers were used instead of the conventional Cardan constraints, in line with other human models [15, 17–19]. In particular, Cardan stiffness was replaced by the proportional component of the PID controller, while the derivative component replaced Cardan damping. In the absence of the integral controller, a head pitch rotation of 6.4 degrees was observed, and also the trunk moved forward. The PID framework's integral actions effectively mitigated drift tendencies while maintaining the necessary dynamic response (see Fig. 3 right). The drift could also be resolved with high joint stiffness values, but this resulted in a poor model fit where, in particular, the head rotations were underestimated by the model.

2.3.1 Head in space control (HiS)

The PID controllers described above stabilize each joint degree of freedom separately [56–60]. Neck postural stabilization is also governed by visual and vestibular feedback of head rotation in space [40]. This was implemented in the EHM with additional feedback loops for head pitch and roll rotation in space, actuating the upper and lower neck joints, and an equivalent loop for head yaw control in space controlling upper neck yaw. This resulted in

5 HiS loops, each having three gains (PID). However, in the current study, only D actions representing feedback of head rotational velocity were needed to obtain a good fit. HiS P and I actions will be more relevant in conditions with substantial seat rotation [41]. The HiS loops assume perfect perception of 3D head rotation in space, which was shown to be an acceptable simplification of models capturing sensory integration of visual and vestibular motion perception when simulating postural stabilization of the neck [41].

3 Validation and parameter estimation

3.1 Experimental Data for Model Validation

The validation of the models involved utilization of experimental data obtained from a study conducted in our lab with an experimental compliant seat with adjustable back supports [7]. From the 18 participants in the original dataset, we selected 10 mid-size participants (73.7±9.0 mean±std kg, and 1.753±0.067 m standing height, 4 male, 6 female) matching the EHM body size and used responses averaged in the time domain over these participants for model validation. From this dataset, three conditions were selected: 1) high support-erect posture, 2) low support-erect posture, and 3) high support-slouched posture. Here "*high support*" includes two rectangular foam cushions (see Fig. 4 left), and "*low support*" only includes the lower cushion (Fig. 4 right). For high support, we studied erect and slouched postures, whereas for low support, we studied the erect posture. The lower support pad is located at the posterior superior iliac spine. The high support is aligned with the apex of the scapula's angulus inferior. To simulate real-world scenarios, participants were instructed to sit in a car mock-up, where they were subjected to random vibrations in vertical, fore-aft, and lateral directions. To capture and record 3D full-body kinematic data (translational and rotational), participants wore a motion capture suit with seventeen triaxial inertial measurement units (IMUs) at 240 Hz (MTW Awinda, Xsens Technologies, Enschede, The Netherlands). Through integration, the Xsens software reconstructs orientations of all body segments and the quasi-global positioning of their joints. These sensors were crucial in

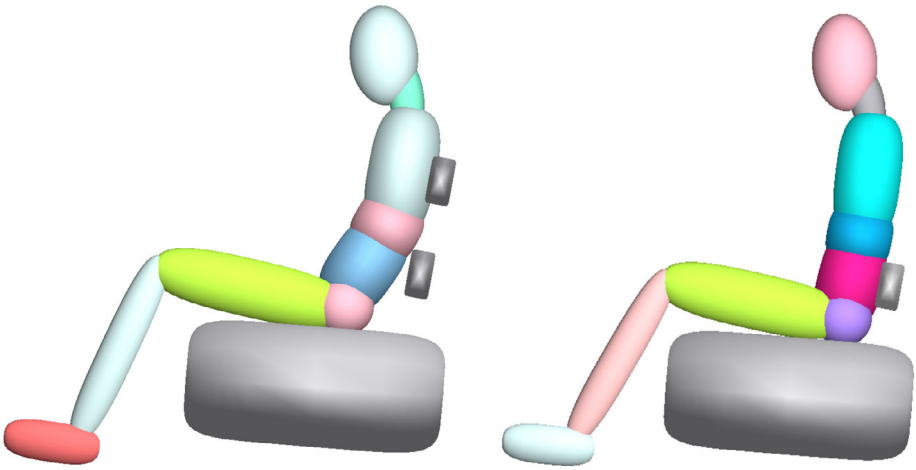

Fig. 4 Slouched posture with a high backrest (left) and erect posture with a low backrest (right)

Table 3 Erect versus slouched postures. The angle between the horizontal plane and the connecting line between the pelvis and thorax (T8)

	Erect (Degrees)	Slouched (Degrees)
Experiment	66.22	53.74
Model	65.01	53.57

collecting comprehensive information, including the position, velocity, and acceleration of various body segments throughout the experimental sessions. Attaching sensors with a body suit may result in a mass-spring-damper effect, potentially distorting measurements at high frequencies, particularly in the trunk and pelvis. Additionally, the sensor fusion algorithms, which balance dynamic response and accuracy, may increase drift in dynamic scenarios due to accelerometer and gyroscope-induced integration issues. These limitations highlight the need for careful interpretation and suggest areas for future improvement in human body vibrational response measurement methodologies using IMUs. This dataset was subsequently utilized to validate the model. For each posture, the body was rotated such that the angle between the horizontal plane and the connecting line between the pelvis and thorax (T8) matched the experimental values presented in Table 3.

3.2 Parameter estimation

As mentioned before, the parameters of the human body, such as mass and inertia value, are predefined according to a 50th percentile male body size. To establish the joint stabilization parameters, we employed parameter identification methods fitting the EHM response to human response data for vibration transmission from the seat base to the human body. In the same procedure, multibody seat and seat back contact parameters were also fitted to the human response data. These contact parameters represent compression and shear and are described in Sects. 4.1 and 4.2.

3.2.1 Objective criteria

The head, pelvis, and trunk motion in translation (vertical, fore-aft, and lateral) and rotation (roll, pitch, yaw) should all be well represented by the model in order to accurately reflect the real human data from the experiments [7]. To that end, gains (head, trunk, pelvis) of various body segments in the frequency domain will be assessed as response functions. The frequency-dependent gain is defined as:

$$\text{gain}_j = \frac{\Phi(s_{o,j})}{\Phi(s_i)} \tag{1}$$

wherein j is the body segment (head, trunk, and pelvis); s_o is the human response of specific body segments in the time domain, such as pelvis's vertical displacement or head's pitch; s_i stands for the input vibration applied at the seat in the time domain; the term Φ refers to the Fourier transform. For the EHM to have enhanced prediction capabilities, the criteria are defined as the relative errors between the model gains from (Eq. (1)) and the experimental gains [7]. The gains considered as criteria for the model fitting under various seat motions are displayed in Table 4. The experimental data included wideband perturbations with power concentrated between 0.1 and 12 Hz, applied over 60 seconds plus 5 seconds phase in. Coherence and power were quite low at the lowest frequencies and highest frequencies (see Fig. 15–Fig. 17 in the Appendix). Hence, we used gains from 0.18-8 Hz in

Table 4 Gains considered for parameter estimation and validation

	Fore-aft seat motion	Lateral seat motion	Vertical seat motion
Fore-aft displacement	✓		
Lateral displacement		✓	
Vertical displacement			✓
Roll motion		✓	
Pitch motion	✓		✓
Yaw motion		✓	

fore-aft loading, 0.36-8 Hz in lateral loading, and 1–10 Hz in vertical loading for model fitting. The transfer function estimate is computed using MATLAB's "Tfestimate" function [64]. In each seat motion condition, the gain of the experiment as a function of frequency is denoted as $Gain_{exp}$ and the gain of model as function of frequency is denoted as $Gain_{model}$. For each frequency f the mismatch between $Gain_{exp}(f)$ and $Gain_{model}(f)$ is scaled towards a reference gain ($Ref_{Gain}(f)$), based on the experimental gain:

$$Ref_{Gain}(f) = Gain_{exp}(f) + 0.05\overline{Gain}_{exp} \tag{2}$$

Here, the term $0.05\overline{Gain}_{exp}$ is added to reduce the effect of very small gains on the overall criterion. The Fourier transform results in a few low frequencies and many high frequencies. To create a balanced fit across frequencies, we have given higher weight to lower frequencies by dividing the error ($Gain_{exp}(f) - Gain_{model}(f)$) with the corresponding square of frequencies. The error criterion ($RMS : root\ mean\ square$) for each individual objective function is thus formulated as:

$$Crit_j = RMS\left\{\frac{Gain_{exp}(f) - Gain_{model}(f)}{Ref_{Gain}(f)\ f^2}\right\} \tag{3}$$

3.2.2 Optimization procedure

To replicate the experimental conditions, we used the same input signal as the one experienced by the participants during the experiment. Figure 5 shows the vibrational vertical input seat excitation; similar inputs were applied to the fore-aft and lateral directions. For initialization towards equilibrium in Madymo (i.e., the human body sinks into the seat), no excitation was provided for the first 5 secs. The vibrational excitations to the seat were given after that.

The optimization process is required to strike a balance between the number of function evaluations and the accuracy of the solutions obtained. For the combined validation in fore-aft, lateral, and vertical motion, Table 4 selected seven main signals, which were evaluated for three body segments (head, trunk, pelvis), resulting in 21 objective criteria to optimize. With fore-aft and vertical seat motion, there are no lateral, roll, and yaw responses, and hence, these are not considered. Fore-aft responses with vertical seat motion and vertical responses with fore-aft seat motion are limited and therefore not considered. With lateral seat motion, the fore-aft and vertical responses were minor and therefore also not considered.

For this multi-objective optimization problem, we were looking for solutions that represent trade-offs between the different objectives. Balancing the accuracy of solutions across

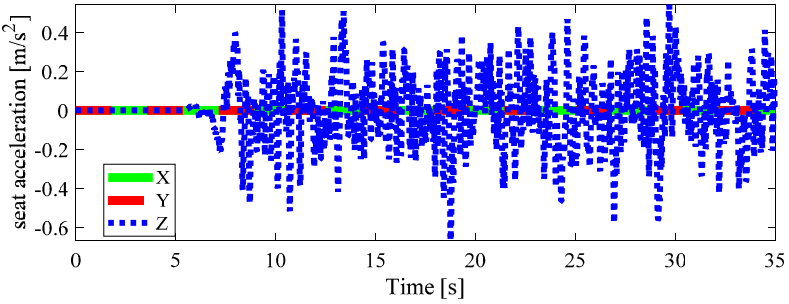

Fig. 5 Seat input excitation/acceleration for vertical loading case, with settling (0-5 s), phase-in (5-10 s) followed by a continuous wideband perturbation (No x and y accelerations)

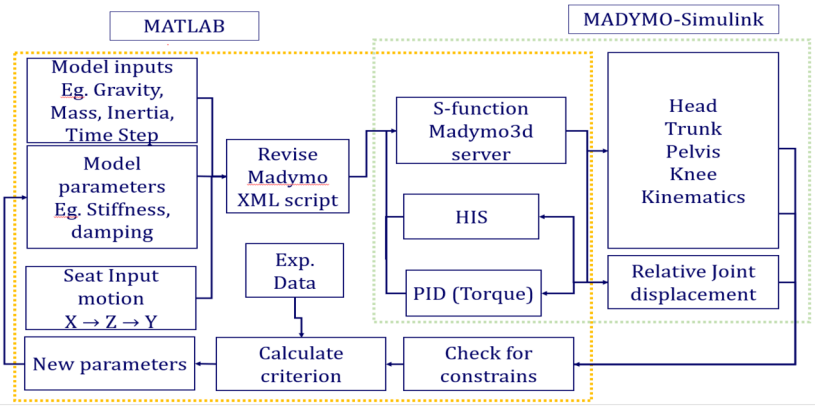

Fig. 6 MATLAB - Madymo-Simulink co-simulation and optimization architecture

multiple objectives is particularly challenging. The Madymo-Simulink simulation and optimization architecture are shown in Fig. 6. MATLAB was used to create and maintain the model, analyze the results, and estimate parameters, whereas Simulink was utilized to execute the simulation. Simulink is used to define the PID and HiS controllers, which offer more flexibility than Madymo controllers. Simulink calls the Madymo mechanical, human body, and seat model, using an S-function to interface the MATLAB and Madymo servers. It allows the Madymo server to send data to the Simulink server and vice versa. The Matlab functions textscan, strfind, and fprintf are used to adapt the model parameters which are contained in the xml file representing the MADYMO model. The experimental data is used to train the optimization algorithm. The Madymo-Simulink simulation and optimization architecture is a versatile, powerful, flexible, and reliable tool that is used to optimize different conditions. It is used to find accurate and efficient solutions to optimization problems, and it can be adapted to different applications. This Madymo-Simulink simulation and optimization architecture can be used for a variety of research and industrial applications, and it demonstrates a valuable tool for improving the comfort, safety, and efficiency of human-machine systems.

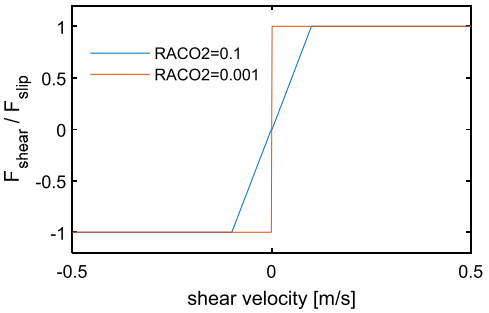

Fig. 7 Approximated stick-slip friction for ellipsoid contact. The contact shear force F_{shear} is limited to the slip force F_{slip}, which equals the normal force multiplied by the friction coefficient. The numerical parameter RACO2 allows slip with a velocity proportional to RACO2. RACO2 = 0 would represent pure stick-slip (Color figure online)

4 Seat modelling

To capture the human body contact with seat cushion, seat back and floor, contacts have been established based on contacting surfaces [65]. Using a master surface (planes and ellipsoids) against a slave surface (ellipsoids), contact interactions are specified to secure body contact at each surface (i.e., feet and floor, pelvis and seat pan, and torso and backrest). In all cases, the floor was modeled as an infinite plane, and the seat base using an ellipsoid. Since the primary focus has been on seat modeling, several seat-back models were evaluated as described in this paper. In future work, we will emphasize the interaction of the feet in more detail.

4.1 Multibody seat model with stick-slip friction

In this model, the seat back is modeled using tenth-order ellipsoids approximating the rectangular foam blocks of the applied experimental seat. The seat cushion is modeled with a sixth-order ellipsoid. All contacting surfaces of the EHM, floor, seat, and seat back are allowed to penetrate each other. The penetration determines the equivalent contact force, defined as linear force-deflection characteristics with stiffness in N/m and damping in Ns/m. As a result, the contact model captures compliance in compression taking into account the 3D geometry of the body and seat. The contact model includes approximated stick-slip friction. This friction model applies a resistive force proportional to the slip velocity with very low slip velocities and a constant resistive force representing friction with higher slip velocities (Fig. 7). This friction model is chosen to enhance computational efficiency but may lead to drift in prolonged simulations. Dynamically, it approximates stick-slip friction well with a breakout friction equal to the slip friction. In the results presented, the transition velocity parameters (RACO-ramp coefficients) are set to RACO1 = 0 (force starts to develop from zero velocity), with the Madymo default RACO2 = 0.1 (force saturates at 0.1 m/s) and with RACO2 values between 0.3 and 1e−5 m/s where lower RACO2 values approximate pure stick-slip friction. RACO, serving as a control element, facilitates the input of time domain analysis data pertinent to the multibody solver, enabling the configuration of analysis duration, time step size, tolerances, and ramp functions. Friction coefficients were chosen to be 1.2 for the flat seat back and 1.6 for the seat base, reflecting the curved seat surface providing additional support. For the feet, a very high friction of 5 was selected as the curved vehicle floor would limit foot motion.

4.2 Multibody seat model with shear deformation

The approximate stick-slip friction could not accurately reproduce vibration transmission through shear forces. Hence, we replaced the stick-slip friction for the seat and seat back

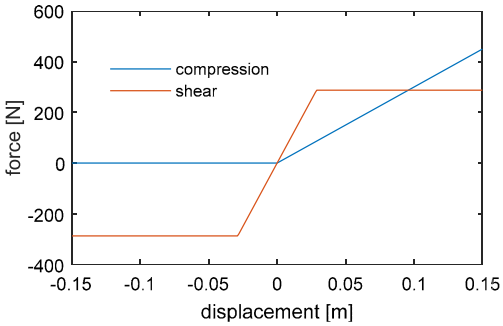

Fig. 8 Contact compression and shear compliance for pelvis-to-seat contact. The nominal compression force is ∼180 N, and assuming friction of 1.6 shear force is limited to 288 N. Compression and shear stiffness are estimated fitting the human response data (Color figure online)

contact with point restraints acting in the plane of the contact surfaces to capture shear. The point restraints consist of perpendicular parallel springs and dampers that connect the desired bodies. Point restraints for the pelvis and thighs act in the fore-aft and lateral directions, while the ones for the backrest [66] act in the lateral and vertical directions. These point restraints capture seat, muscle, fat, and skin shear deformation. These were currently defined as linear force-deflection characteristics with stiffness in N/m, damping in Ns/m, and a limited force to allow contact slip (Fig. 8).

4.3 Multibody model without contact

The EHM model was also validated by removing all seat and floor contact models and implementing equivalent stiffness and damping with spring-damper models, generating force only in compression. These were combined with the contact shear models described above. Hence, all interactions with seat, seat back, and floor were now captured by 3D spring damper models. The backrest models were split into a left and right model at 0.07 m lateral position. Seat-pelvis contact models were placed at 0.86 m lateral position equivalent to the position of the two buttocks ellipsoids.

4.4 Finite element (FE) backrest

An FE backrest was made up of 1523 four-node tetra elements, and foam characteristics were defined using experimental loading/unloading functions, hysteresis slope, and density [33]. Contact was established with a stick-slip friction coefficient of 1.2. FE was only applied for the backrest, whereas for the seat base, the multibody (ellipsoid) contact with a stick-slip friction coefficient of 1.6 was maintained.

5 Benchmarking EHM, AHM, and seat modeling strategies

The seat-to-head vibration transmissibility depends on the characteristics of the seat and the human body, such as the contact area, pressure, friction, and deformation in compression and shear. The computationally efficient human body model (EHM) described above is evaluated using several contact models and interacting with finite element (FE) and MB backrest models. This is done for the high backrest with erect posture data. In addition, the AHM was evaluated with an FE seat back model, which was shown to well capture vibration transmission and dynamic driving [33].

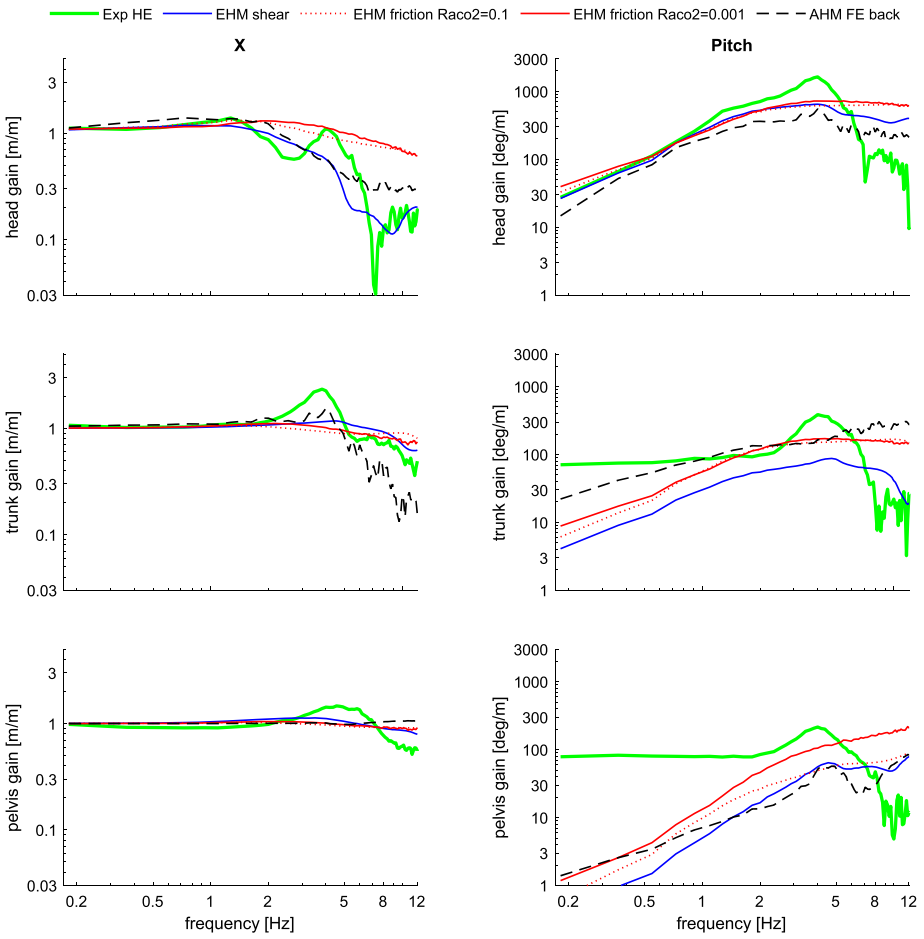

Fig. 9 EHM versus AHM and effect of seat model in fore-aft excitations (high erect) (Color figure online)

5.1 Results EHM vs. AHM and seat models

Figure 9–Fig. 11 show results for three vibration directions in the condition with high backrest and erect posture. Further information on the AHM validation with FE backrest model can be found in [33]. Model errors are shown in detail in Table 5, including further model variations. Results illustrate that both the EHM with shear in the contact interaction and the AHM with FE back rest provide realistic results. In fore-aft and lateral loading, the EHM with shear best captures head motions, whereas the AHM best captures trunk rotation.

The column "MB shear without HiS" in Table 5 shows that the omission of the head in space controller in the EHM more than doubled the model error averaged over head translational and rotational motion with fore-aft and lateral seat motion.

The column "MB shear locked spine compression" shows that locking the spine translational joint mainly affects vertical accelerations. With the joint unlocked, the model correctly predicts amplification from the pelvis to the trunk and head of the vertical acceleration (Fig. 11). With a locked compression joint, the vertical accelerations of the pelvis, trunk, and

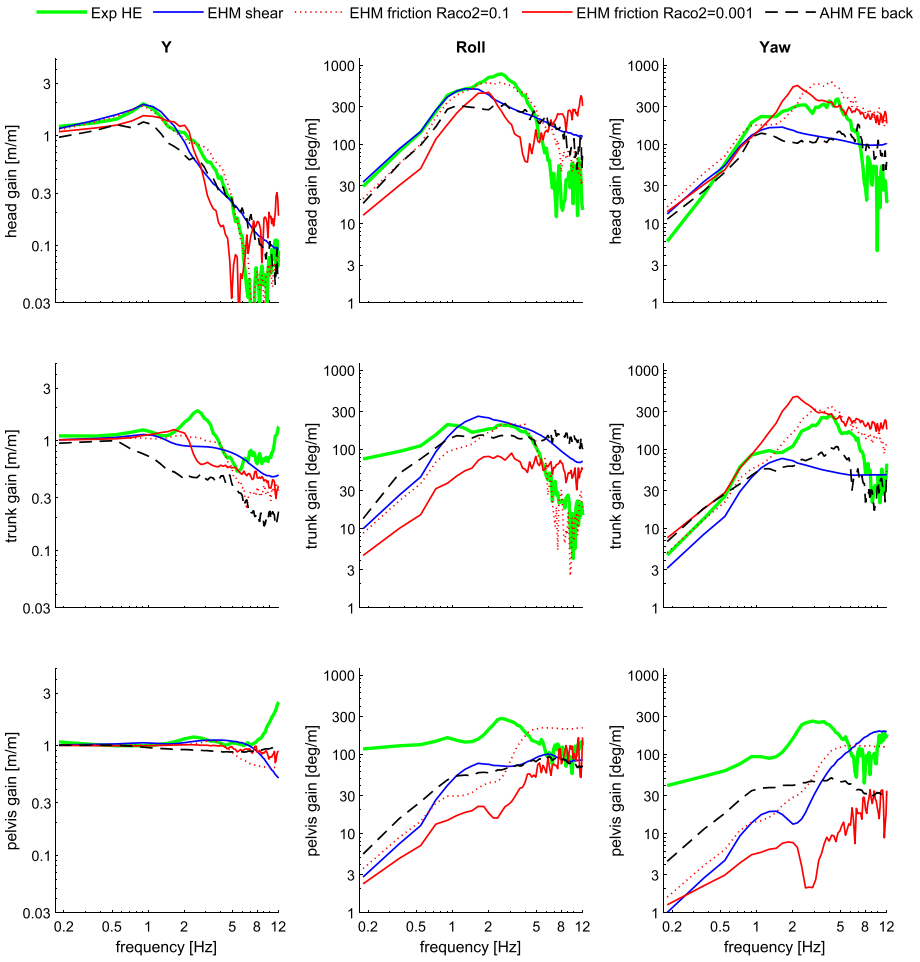

Fig. 10 EHM versus AHM and effect of seat model in lateral excitations (high erect) (Color figure online)

head are nearly identical (not shown), and the model error for vertical acceleration increases with a factor of 3.8 for the pelvis, 2.7 for the trunk, and 8.8 for the head.

The column "MB shear no contact" shows results similar to the model "MB shear" with ellipsoid contact capturing compression and springs capturing shear. The head vertical acceleration is even better predicted (see also Fig. 20 versus Fig. 17 in the Appendix). This illustrates that, for the current validation in vibration conditions, the geometry-based ellipsoid contacts can be replaced well by 3D spring damper models.

The EHM with stick-slip friction contact is the least realistic (see Table 5 and Fig. 9–Fig. 11) with a somewhat lower coherence (see Fig. 15–Fig. 17 in the Appendix). For the contact model with friction, the model error (see Table 5) varied strongly with the numerical slip parameter RACO2 (see Sect. 4.1). This highlights the importance of the applied friction model. RACO2 is a numerical parameter that should be chosen to balance accuracy and computational efficiency and not for model fitting. Lower RACO2 values ($\leq$0.001) approximate stick-slip friction and do not well capture vibration transmission. A reasonable fit

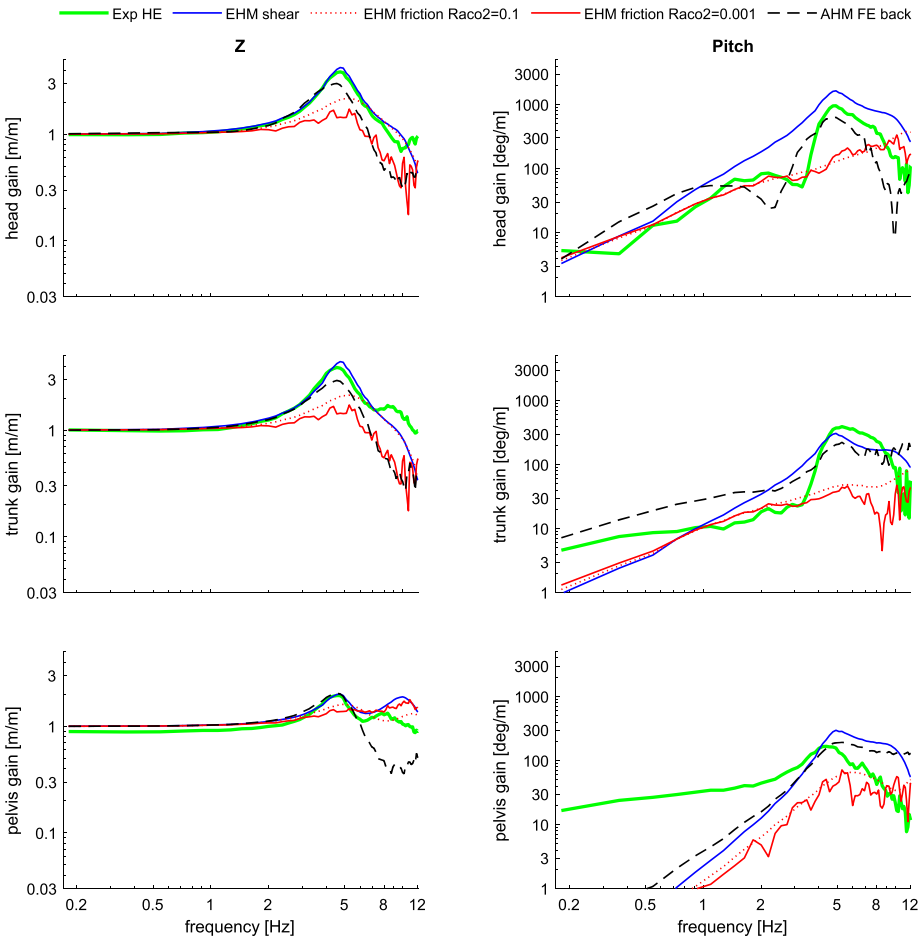

Fig. 11 EHM versus AHM and effect of seat model in vertical excitations (high erect) (Color figure online)

was obtained with RACO2 = 0.1, which creates a sort of shear damping but is not physically plausible and can cause unrealistic drift in prolonged simulations. Apparently, the FE back model and the multibody models with contact shear best capture the dynamic response of the compliant seat and the compliant human body tissues.

5.2 Computational requirements

All simulations were performed on a regular desktop Windows computer with an Intel(R) Xeon(R) W-2223 CPU @ 3.60 GHz and 128 GB of RAM, using the software Madymo Simcenter 2022.1, with the following settings: INT_MTH = "MATLAB," ANALYSIS_TYPE = "DYNAMIC," CONSTRAINT_TOL = "1E-09," RAMP = "0.0 0.5," RACO1 = 0.0, RACO2 = 0.1, as well as other values of RACO2, and utilizing a total of 4 processors. The AHM version 3.3 (31 Aug 2020) was used. Matlab-Simulink was used to control the simulation, using fixed timestep eighth-order Dormand-Prince integration (ode8), which was found to allow a relatively large timestep with good computational efficiency. Variable timestep al-

Table 5 Model error in condition high erect, for each seat motion direction, for relevant gains. The model error is derived with Eq. (3) and represents the relative gain error averaged over all relevant frequencies

	AHM FE backrest	MB friction RACO2 = 0.1	MB friction RACO2 = 0.001	MB shear	MB shear without HiS	MB shear locked spine compression	MB shear no contact
Human model	AHM	EHM	EHM	EHM	EHM	EHM	EHM
Seat back model	FE + friction	ellipsoid + friction	ellipsoid + friction	ellipsoid + shear springs	ellipsoid + shear springs	ellipsoid + shear springs	compression + shear springs
Average error over all motion directions excluding trunk and pelvis rotation							
	0.200	0.286	0.352	0.304	0.344	0.322	0.260
Average error for head motion for fore-aft and lateral seat motion							
	0.203	0.144	0.204	0.120	0.300	0.121	0.185
Fore-aft (X) seat motion							
Head X	0.150	0.191	0.226	0.089	0.167	0.090	0.085
Head pitch	0.268	0.166	0.188	0.132	0.536	0.139	0.168
Trunk X	0.063	0.069	0.060	0.062	0.062	0.065	0.062
Trunk pitch	0.332	0.532	0.509	0.655	0.663	0.659	0.562
Pelvis X	0.078	0.090	0.088	0.102	0.102	0.102	0.114
Pelvis pitch	0.847	0.829	0.800	0.862	0.875	0.863	0.852
Lateral (Y) seat motion							
Head Y	0.253	0.060	0.164	0.101	0.423	0.100	0.063
Head roll	0.322	0.178	0.476	0.119	0.529	0.118	0.100
Head yaw	0.289	0.254	0.228	0.232	0.284	0.232	0.139
Trunk Y	0.317	0.116	0.119	0.114	0.132	0.113	0.064
Trunk roll	0.435	0.581	0.765	0.503	0.441	0.505	0.448
Trunk yaw	0.291	0.211	0.600	0.329	0.327	0.330	0.216
Pelvis Y	0.067	0.042	0.043	0.046	0.040	0.046	0.053
Pelvis roll	0.707	0.781	0.839	0.737	0.726	0.738	0.701
Pelvis yaw	0.572	0.710	0.772	0.721	0.705	0.721	0.561
Vertical (Z) seat motion							
Head Z	0.177	0.166	0.271	0.027	0.041	0.240	0.019
Head pitch	0.258	0.146	0.141	0.768	0.265	0.479	0.396
Trunk Z	0.190	0.201	0.292	0.094	0.105	0.252	0.091
Trunk pitch	0.613	0.130	0.132	0.326	0.255	0.237	0.369
Pelvis Z	0.174	0.111	0.113	0.087	0.107	0.333	0.193
Pelvis pitch	0.606	0.705	0.720	0.658	0.667	0.692	0.634

gorithms could not be used, as they are not supported by the Simulink-Madymo coupling. The applied multibody contact options allowed initial penetration, and a combination of visual positioning and simulations of settling was used to define an equilibrium initial posture and to initialize the integrators of the head in space controller. With FE backrest, large initial penetrations were not allowed, and each dynamic simulation required around 5 seconds of settling at the start.

The EHM with contact shear was stable in all conditions with timesteps of 5E-4 s and lower. Higher timesteps led to excessive rotations in the lower and/or upper neck joints

during initialization, resulting in termination. In particular, the parameters for the head in space controller affected stability. The selected timestep of 5E-4 s provided accurate results with marginal effects of lower timesteps. Only when applied with friction and very low RACO2 values (<1E-3) a lower timestep was needed. The EHM was run using 4 CPUs, leading to total CPU time = 27 s and total elapsed time = 69 s to simulate 35 s, resulting in a real-time factor of 2. Apparently, system overhead initializing, linking Simulink and Madymo, and storing results slow down the simulation process substantially. The effect of overhead was reduced with longer simulations, where simulating 300 s took a CPU time of 102 s, with an elapsed time of 272 s, resulting in a real-time factor of 0.9. The EHM with stick-slip friction was stable with the same timestep, but the results depended more strongly on the applied timestep compared to the EHM with shear. The model "MB shear no contact" where the ellipsoid contacts were fully replaced by spring and damper models, was faster but did not allow a larger timestep. Hence, removing ellipsoid contacts has no major benefits in terms of computational efficiency.

The AHM required a timestep of at most 5E-5 s for numerical stability, where higher timesteps caused instability during initialization. Depending on the initial posture and contacts, elements in the shoulder (clavicle and sternum) and neck region rotated excessively, resulting in termination. This was an initialization problem only. A somewhat higher timestep also resulted in drift, with the full body rolling slightly in the vertical load case. The selected timestep of 5E-5 s provided accurate results with marginal effects of lower timesteps. For the FE backrest, the element size and properties required an FE timestep of at most 2E-4 s for numerical stability. Hence, for the AHM, the FE backrest was run at the same timestep as the AHM multibody components and the FE backrest model took around 20% of the computational effort. The AHM with FE backrest model was run using 4 CPUs, which enhanced processing time due to parallel processing of contacts and FE model sections. This resulted in a total CPU time = 33492 s (9 hours 18 minutes), with total elapsed time = 10050 s (2 hours 47 minutes) to simulate 35 s, resulting in a real-time factor of 280. Using more than 4 CPUs marginally affected the elapsed time.

As the applied vibration was limited to 12 Hz, the applied timesteps of 5E-4 (EHM) and 5E-5 (AHM) seem to offer scope to enhance efficiency. The applied explicit integration might be replaced by implicit integration, allowing for reduced time steps.

6 Validation EHM for low back support and slouched

This section evaluates the EHM using the most efficient seat compliance model, which uses ellipsoid contact in conjunction with spring-damper models to capture shear. This seat compliance model is described in Sect. 4.2 and compared to other seat models in Sect. 5.1. We explored how different postures and back supports affect the body's response to vibrations, emphasizing the influence of muscle activation patterns. The parameter optimization was conducted separately for the three posture and back support conditions.

With low erect posture, higher lumbar position and velocity gains KP and KD were estimated in particular in pitch, which is not surprising as the upper back was no longer supported, requiring active lumbar stabilization (see Table A1 for parameters). Higher lumbar KP and KD in pitch were also estimated in the slouched posture, where they presumably represent increased passive resistance in the nonlinear part of the spinal joint range of motion. Our current study estimates a position gain of 200-742 Nm/rad for the 2 lumbar joints J3 and J4. Hence, the combined stiffness of these 2 lumbar joints ranges from 100–371

Nm/rad. These lumbar pitch gains can be compared to parameters estimated in [54] for dynamic perturbation experiments in seated participants with their pelvis fixed and the back unsupported. This study separately estimated a lumbar stiffness k ranging from 100–150 Nm/rad and a position feedback gain k_p ranging from −50 to +50 Nm/rad (Fig. 8 in [54]). The sum $k+k_p$ is comparable to our parameter KP in lumbar pitch and illustrates that the parameters are in the same range. Likewise, our lumbar pitch KD ranges from 24-200 Nm/rad for the 2 lumbar joints J3 and J4, resulting in 12–100 Nm/rad for the combined joints. This range is comparable to the damping b ranging from 8–40 Nm/rad plus k_v ranging from 10-40 Nm/rad (Fig. 8 in [54]).

The neck stabilization parameters and spinal compression parameters were almost the same for the three conditions. The estimated seat and seat back compression parameters were also quite similar. The neck pitch HiS parameters can be compared to our detailed neck model study, where the HiS velocity gain was estimated to range from 0.55–2.4 Nm/(rad/s) (G_{sc} in Table 1 in [55]). The current paper estimates similar HiS pitch KP gains for the lower and upper neck ranging from 1.31-2.21 Nm s/rad.

The experimental vs. model results for three different vibration directions are presented in Fig. 12–Fig. 14 for the MB seat model with shear and in Fig. 18–Fig. 20 (see Appendix) for the MB seat model without contact. For both seat models, results are similar, and overall, a good correspondence is obtained for head translation and rotation. Trunk and pelvis translation are predicted quite well, but the rotations predicted by the EHM at the lowest frequencies are below the experimental rotations, in particular, for the pelvis. This is also the case for the AHM (see Fig. 9–Fig. 11) and may also relate to inaccuracies in the experimental data, where IMUs are not the most robust option to estimate low-frequency rotation. The EHM, in most cases, also predicts the correct trends between the three posture and back support conditions.

7 Conclusion

This study presented a comprehensive and innovative approach to address the challenges of predicting and optimizing vehicle vibration (dis)comfort. The research focused on the development of a three-dimensional (3D) computationally efficient human body model (EHM) that accurately captures human motion, posture (erect/slouched), and backrest support (low/high) during vehicle travel, particularly under vibrations in different directions (fore-aft/lateral/vertical). The EHM was designed through a meticulous process, considering various body segments, multibody/FE contacts, and joint configurations, and was fine-tuned using stepwise optimization techniques. The integration of efficient body modeling, postural adjustment techniques, contact point restraints, and modeling strategies, such as HiS and PID joint controllers, facilitated accurate and efficient prediction of human responses to vehicle vibrations.

Future work could involve integrating whole-body active muscle controllers, visual-vestibular motion perception [41], and more advanced postural stabilization models to enhance the model's ability to capture complex human responses, including anticipation. The model now includes the arm mass into the trunk body, and model variations show that this notably affects vertical vibration transmission. The model can be refined by redistributing the trunk mass, including separate arm models, with a flexible connection mimicking the translational flexibility of the shoulder girdle and modeling the flexible connection of soft tissues, in particular, in the abdomen towards the spine. Spinal compression was captured

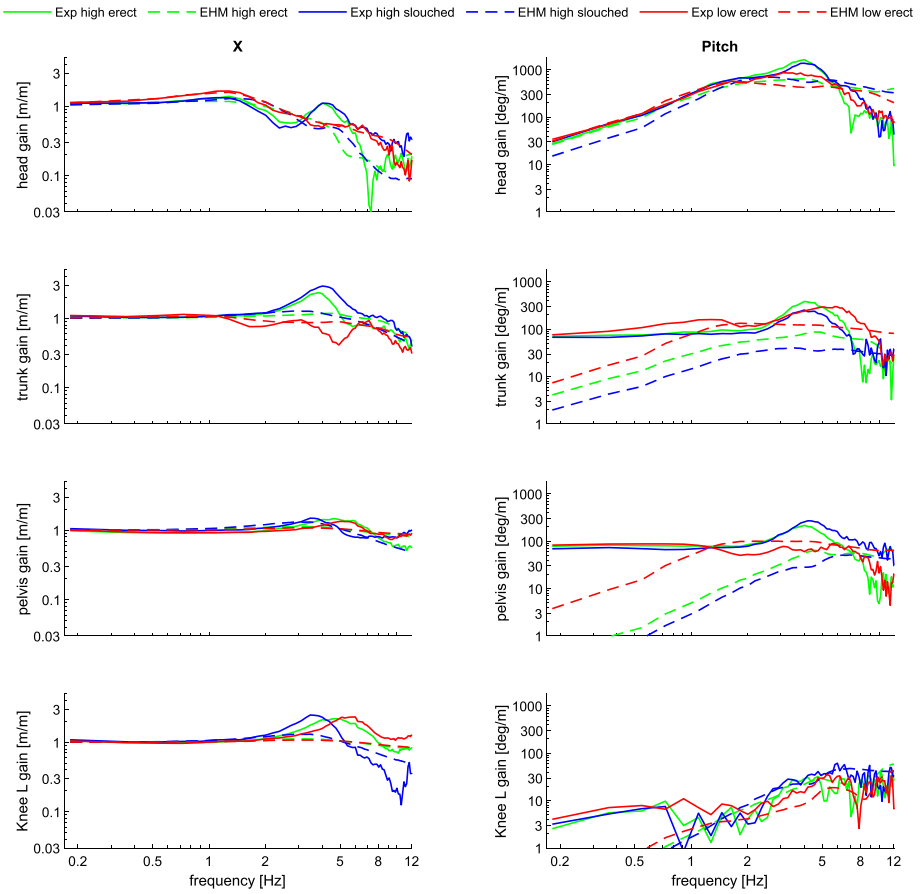

Fig. 12 Experiment vs. EHM model in fore-aft loading in 3 postures, with MB seat model with shear [Units: translational gain (m/m) and rotational (deg/m)] (Color figure online)

with one translational degree of freedom in the lumbar spine and can be refined with additional degrees of freedom in the lumbar, thoracic, and cervical spine [63]. Such details will be particularly relevant for vertical vibration transmission at higher frequencies but will hardly affect low-frequency dynamics related to motion sickness.

The model fitting may benefit from using the measured seat and seat back pressure and shoulder motion in the validation and fitting process. The seat center of pressure may help fit the contact stiffness for the thighs and pelvis. The seat back force can help distribute the stabilizing effects of hips, lumbar joints, and seat back contact. Here, using static seat and seat back forces will be already beneficial, and as a next step, frequency analysis for seat and seat back contact force may support fitting and validation (see Figs B.1 and B.2 in [7]). The back contact shear parameters strongly affected the lateral and vertical conditions. Initially, they were estimated using the lateral case, resulting in considerable damping, which reduced the 5 Hz oscillation in vertical. This was resolved by fitting back contact shear to the vertical case. The lateral case could still be fitted, adapting the hip and lumbar parameters, with a somewhat reduced model fit for the trunk.

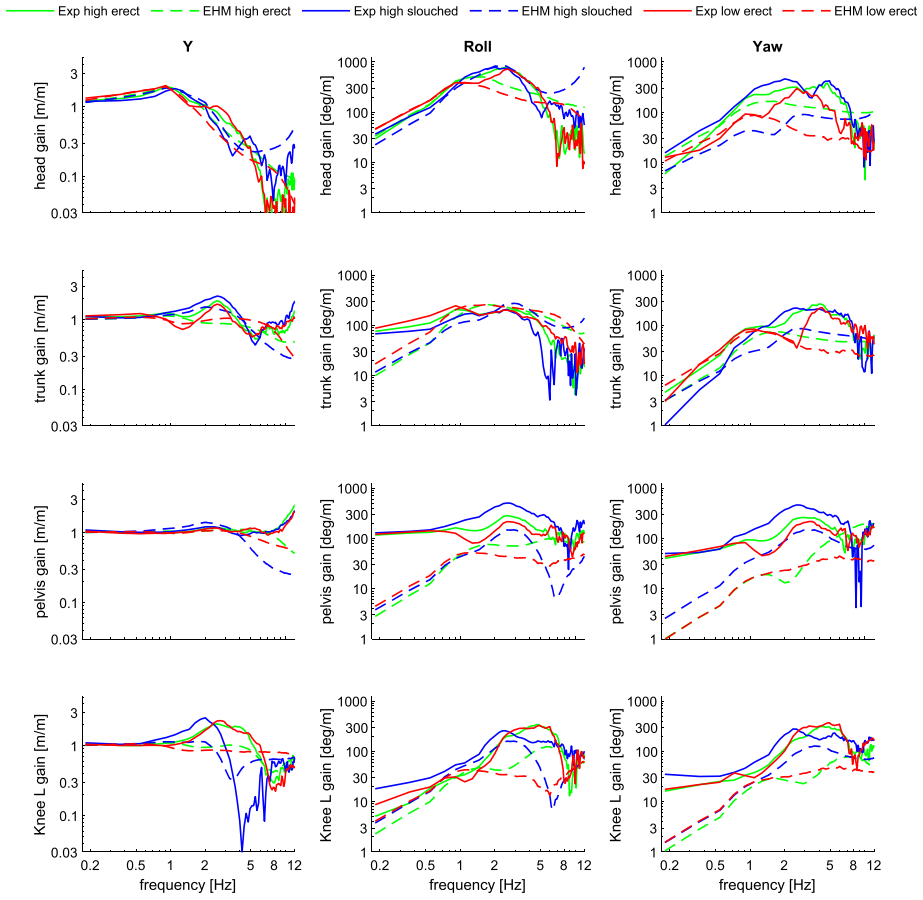

Fig. 13 Experiment vs. EHM model in lateral loading in 3 postures, with MB seat model with shear [Units: translational gain (m/m) and rotational (deg/m)] (Color figure online)

The AHM with FE backrest was found to be accurate but computationally expensive, while the multibody EHM with contact shear is even more accurate and faster than in real-time. The high accuracy of the EHM demonstrates that a relatively simple 3D full-body model can capture vibration transmission. However, the good fit of the human data achieved with the EHM also relates to the limited computation cost, which allows for effective model fitting. Future studies shall demonstrate the accuracy of the EHM and seat models in broader conditions. Validation results are shown for 0.18–12 Hz where only frequencies up to 8 Hz were used for model fitting in horizontal loading and up to 10 Hz in vertical loading. The validation employed IMUs (XSENS) strapped to the body. Validation at higher frequencies will benefit from additional measurements, such as using a mouth-held bite bit.

The seat and contact model evaluation demonstrated the well-known importance of the compression dynamics of the seat and the human body. It also demonstrated the relevance of shear deformation and friction in vibration transmission. Simple stick-slip friction models were found inadequate, and only with contact models capturing shear a good model fit was obtained. This calls for further measurement and modeling efforts of compliance, as well as shear and friction interactions of the human body with compliant seats [67]. Ideally,

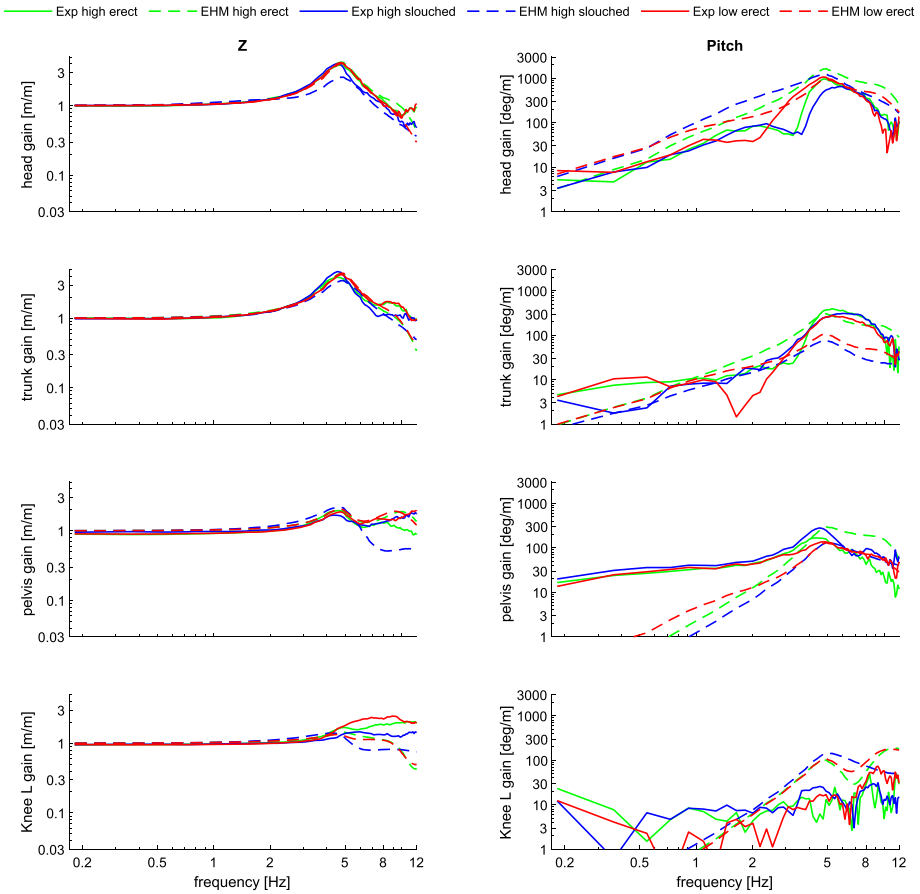

Fig. 14 Experiment vs. EHM model in vertical loading in 3 postures, with MB seat model with shear [Units: translational gain (m/m) and rotational (deg/m)] (Color figure online)

shear forces and displacements could be measured to support modeling shear deformation, which was shown to be essential in vibration transmission. However, this creates an essential technical challenge in measuring shear in human soft tissues and seats where clothing may affect the shear interaction.

The study also delved into the importance of posture in ride comfort analysis and highlighted the role of seat interactions, joint definitions, and stabilization mechanisms in enhancing the accuracy of the model. Joint stabilization was achieved through a strategic combination of passive joint resistance and active muscular, joint stabilization, resulting in a biomechanical framework that enabled precise prediction and analysis. Furthermore, the research provided valuable insights into the parameter identification process, optimization framework, and objective criteria used for model validation. The approach adopted a balance between computational efficiency and accuracy, ensuring that the resulting model was both practical for real-world applications and capable of accurately representing human responses. By accurately simulating human reactions to vibrations and movements, the EHM can contribute to designing and optimizing comfortable and safe automated vehicles.

Its real-time capability allows in-vehicle applications, actively controlling vehicle and seat motion to enhance comfort.

The applied seat models are relatively simple, and more detailed seat models may be more suitable for supporting the design of seat shape and compliance. However, the simplicity of the applied seat models will be an advantage in other applications. As shown in this paper, seat contact compliance and shear parameters can be efficiently estimated without detailed knowledge of the seat using a simple 3D vibration experiment with human subjects. This makes such models suitable for capturing seat dynamics when designing vehicle motion and active seat controllers.

Appendix

Table A1 Parameters estimated for the EHM model with shear. KP = position feedback gain [Nm/rad], KI = Integrator gain [Nm/rad s], KV = velocity feedback gain [Nm s/rad]. * upper and lower neck HiS pitch KP were chosen to be identical to simplify the parameter estimation. Spine compression and contact stiffness are in N/m and damping in N s/m

Parameter	High Erect (HE)	Low Erect (LE)	Slouched
knee KP	783.4	783.4	783.4
knee KD	29.6	29.6	29.6
hips internal rot KP	906.7	853.2	100.0
hips internal rot KD	5.0	6.8	192.2
hips flexion KP	560.8	199.7	180.4
hips flexion KD	34.9	22.3	200.0
hips adduction KP	998.6	50.0	50.0
hips adduction KD	7.3	180.7	162.9
hips flexion KI	75	75	75
lumbar roll KP	559.3	332.6	467.5
lumbar roll KD	24.5	5.4	93.9
lumbar pitch KP	200.0	742.1	655.2
lumbar pitch KD	24.2	184.3	200.0
lumbar yaw KP	954.7	490.0	205.1
lumbar yaw KD	5.0	88.0	47.2
lumbar pitch KI	55	55	55
spine compression stiffness	2.84E+04	2.58E+04	5.00E+04
spine compression damping	1.48E+01	2.57E+02	4.21E+02
upper neck roll KP	29.5	30.1	28.2

Table A1 (*Continued*)

Parameter	High Erect (HE)	Low Erect (LE)	Slouched
upper neck roll KD	3.0	2.8	2.2
upper neck pitch KP	24.7	24.7	28.3
upper neck pitch KD	16.9	17.1	15.7
upper neck yaw KP	30.3	30.0	19.9
upper neck yaw KD	11.4	11.4	12.4
lower neck roll KP	29.1	21.4	49.9
lower neck roll KD	2.2	2.2	1.9
lower neck pitch KP	24.7	24.7	28.3
lower neck pitch KD	14.6	12.9	15.9
upper neck pitch KI	2.8	2.8	2.8
lower neck pitch KI	2.8	2.8	2.8
upper neck HiS roll KP	0	0	0
upper neck HiS roll KI	0	0	0
upper neck HiS roll KD	4.72	4.73	3.78
upper neck HiS pitch KP*	2.21	5.21	1.31
upper neck HiS pitch KI	0	0	0
upper neck HiS pitch KD	20.55	19.55	18.74
upper neck HiS yaw KP	0	0	0
upper neck HiS yaw KI	0	0	0
upper neck HiS yaw KD	0.026	0.025	0.101
lower neck HiS roll KP	0	0	0
lower neck HiS roll KI	0	0	0
lower neck HiS roll KD	5.31	5.31	5.87
lower neck HiS pitch KP*	2.21	5.21	1.31
lower neck HiS pitch KI	0	0	0
lower neck HiS pitch KD	6.63	6.63	5.18
pelvis contact stiffness	42444	50000	12449
pelvis contact damping	412.5	134.9	41.8
seat back stiffness	1043.9	564.0	1100.2
seat back damping	2.4	1007.4	127.6
thighs contact stiffness	5000	5000	10000
thighs contact damping	511.8	500.0	191.6
upper back shear stiffness	1375	na	3000
upper back shear damping	1000	na	1000
lower back shear stiffness	5574.1	1288.5	7912.2
lower back shear damping	1684.3	540.4	79.6
pelvis shear stiffness	3000	200	3000
pelvis shear damping	500	1000	600
thighs shear stiffness	3000	1950	3000
thighs shear damping	500	1000	600
feet contact stiffness	20000	20000	20000
feet contact damping	1000	1000	1000

Additional plots

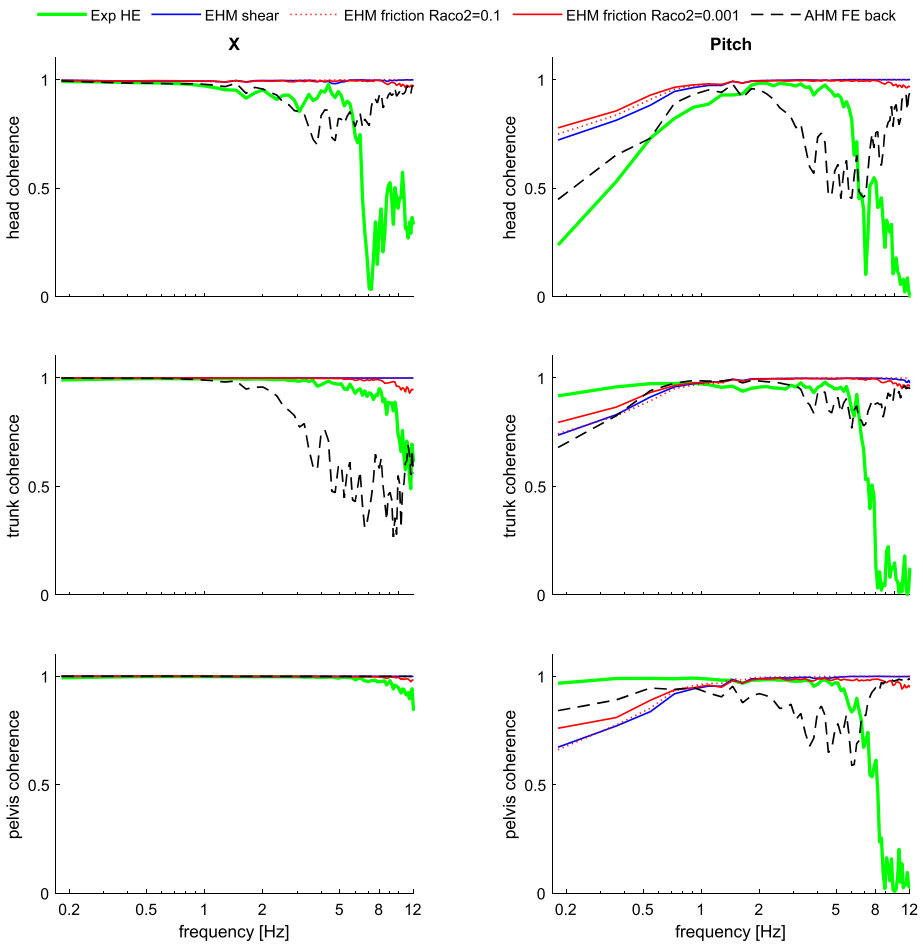

Fig. 15 Coherence EHM versus AHM and effect of seat model in fore-aft excitations (high erect)

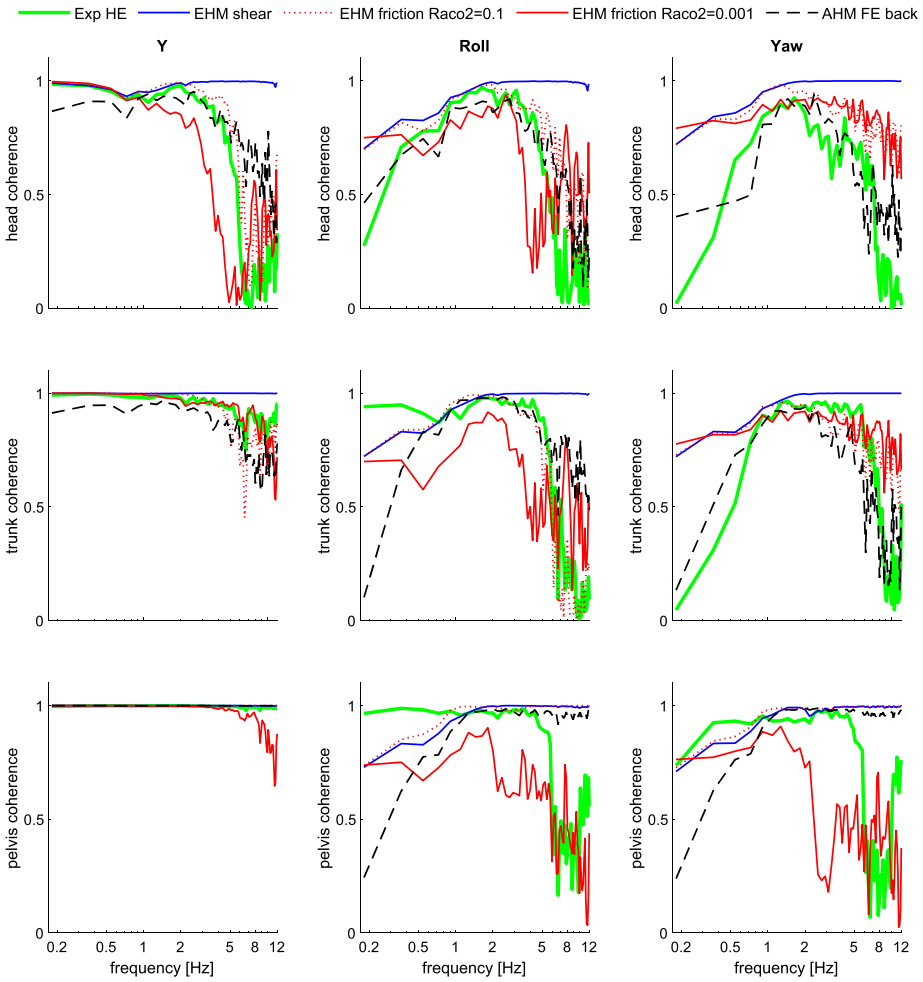

Fig. 16 Coherence EHM versus AHM and effect of seat model in lateral excitations (high erect) (Color figure online)

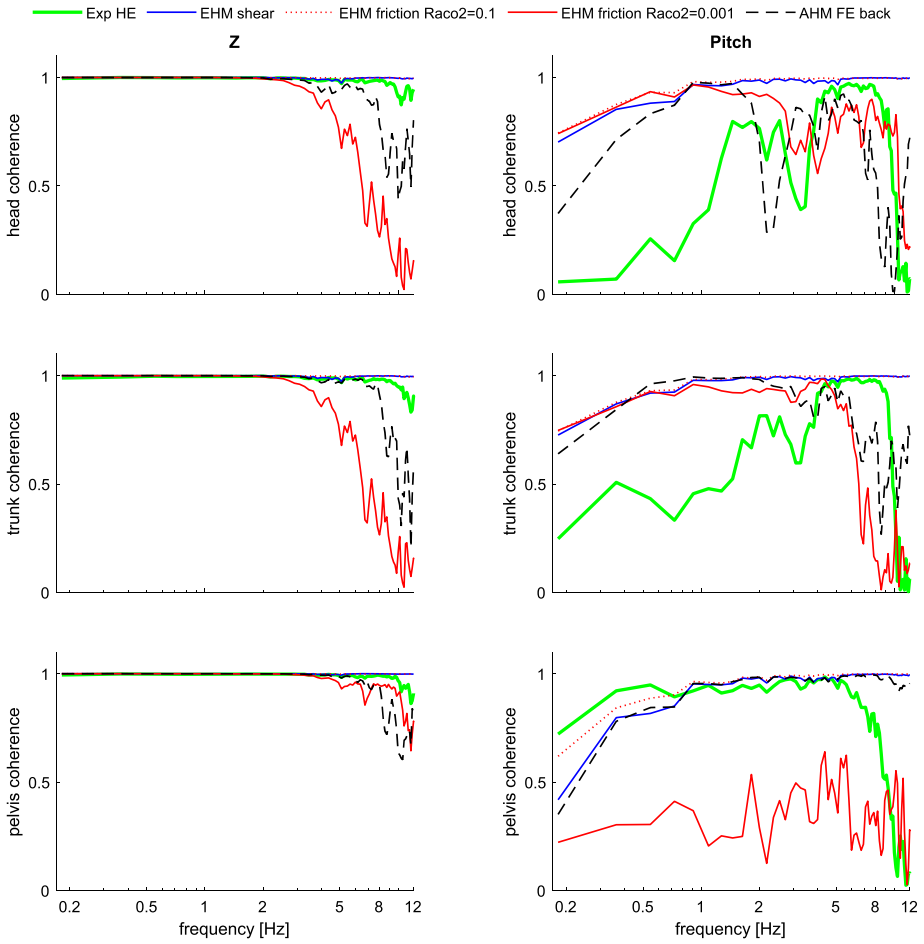

Fig. 17 Coherence EHM versus AHM and effect of seat model in vertical excitations (high erect) (Color figure online)

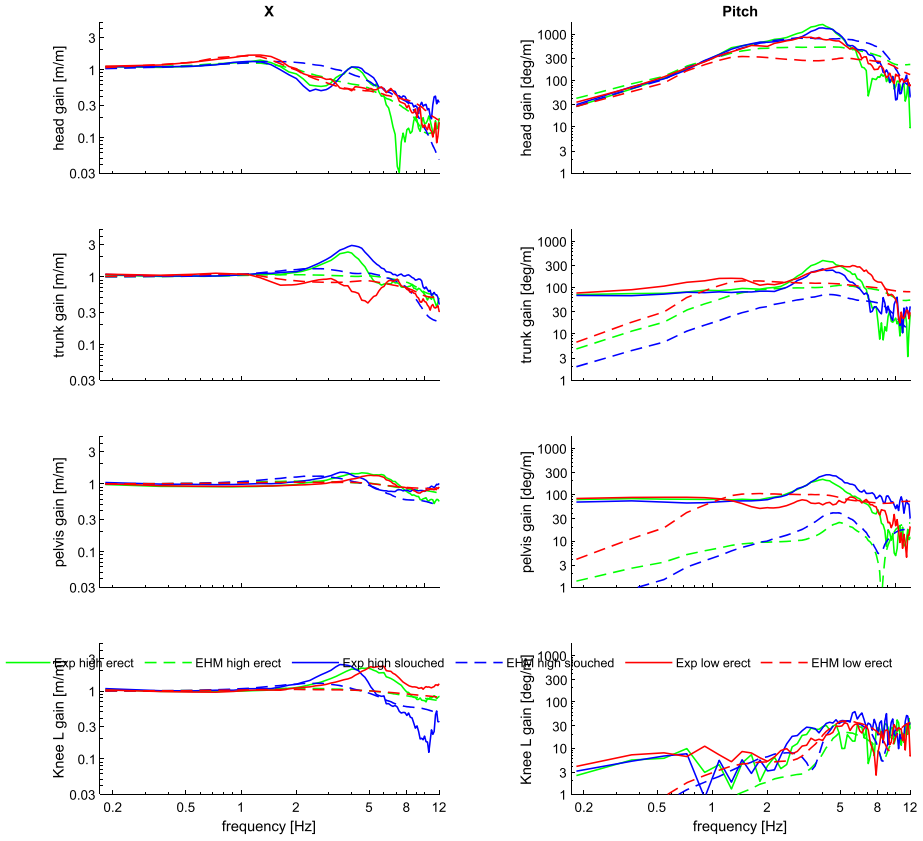

Fig. 18 Experiment vs. EHM model in fore-aft loading in 3 postures, with MB seat model without contact [Units: translational gain (m/m) and rotational (deg/m)] (Color figure online)

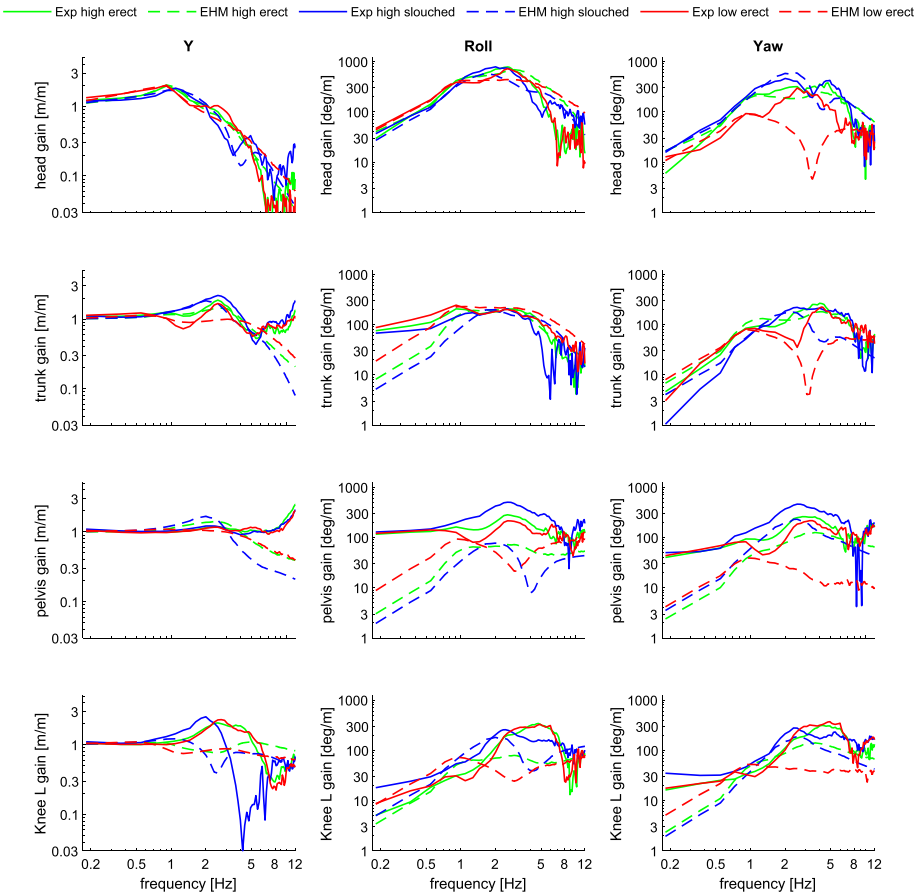

Fig. 19 Experiment vs. EHM model in lateral loading in 3 postures, with MB seat model without contact [Units: translational gain (m/m) and rotational (deg/m)] (Color figure online)

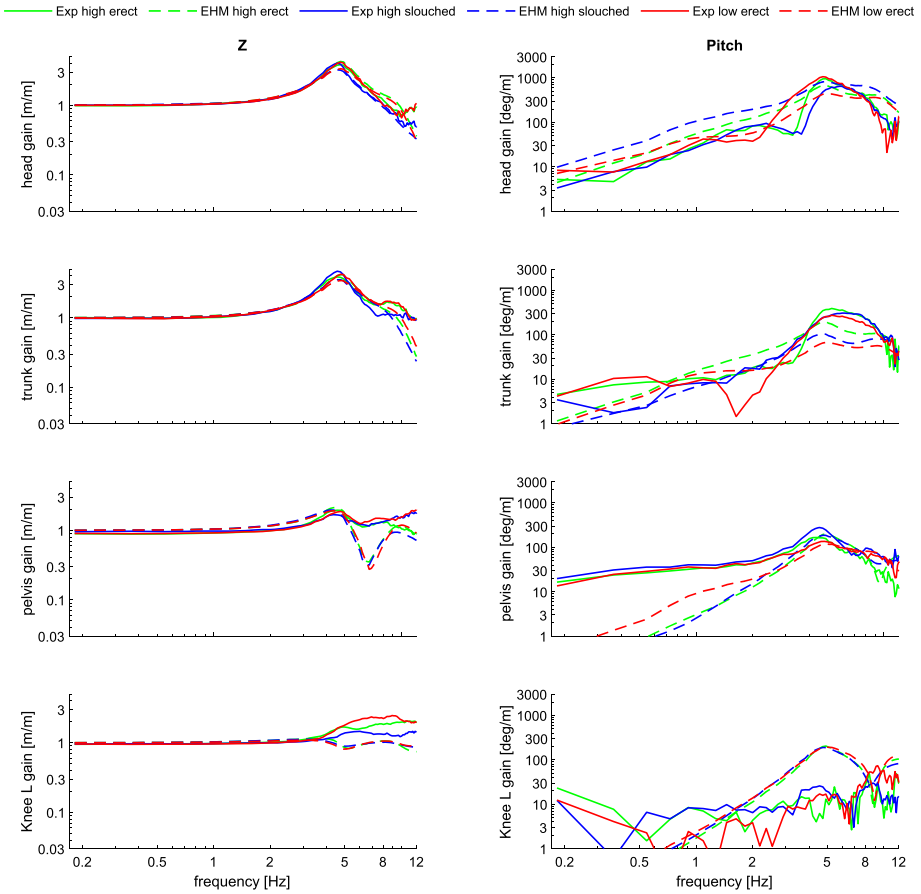

Fig. 20 Experiment vs. EHM model in vertical loading in 3 postures, with MB seat model without contact [Units: translational gain (m/m) and rotational (deg/m)] (Color figure online)

Acknowledgement The research was supported by Toyota Motor Corporation.

Author contributions Raj Desai played a crucial role in this research paper by leading the model-building and optimization processes. He carefully put together the manuscript, using his extensive knowledge and experience. His contributions included review, editing, drafting the manuscript, creating visualizations, validation, methodology, investigation, formal analysis, data curation, and conceptualization. Georgios Papaioannou contributed to the conceptualization and was involved in the review and editing of the writing. Riender Happee contributed extensive expertise to this project, particularly in fine-tuning the model. Riender was instrumental in refining the research narrative and providing essential insights during the conceptualization phase. He participated in conceptualization, funding acquisition, methodology, project administration, resource provision, supervision, and writing – review and editing. Collectively, each author's distinctive contributions were vital to the success of this project. Raj Desai, Georgios Papaioannou, and Riender Happee collaborated seamlessly, resulting in a comprehensive and well-crafted manuscript that reflects their diverse talents and collective commitment to advancing the field. All authors have given their approval for the final version of the manuscript.

Data Availability No datasets were generated or analysed during the current study.

Declarations

Competing interests The authors declare no competing interests.

References

1. Rahmatalla, S., DeShaw, J.: Predictive discomfort of non-neutral head–neck postures in fore–aft whole-body vibration. Ergonomics **54**, 263–272 (2011)
2. Amari, M., Perrin, N.: Whole-body vibration exposure in unfavourable seated postures: apparent mass and seat-to-head transmissibility measurements in the fore-and-aft, lateral, and vertical directions. Ergonomics **66**, 136–151 (2023)
3. Nawayseh, N., Alchakouch, A., Hamdan, S.: Tri-axial transmissibility to the head and spine of seated human subjects exposed to fore-and-aft whole-body vibration. J. Biomech. **109**, 109927 (2020). https://doi.org/10.1016/j.jbiomech.2020.109927
4. Mansfield, N.J., Maeda, S.: The apparent mass of the seated human exposed to single-axis and multi-axis whole-body vibration. J. Biomech. **40**, 2543–2551 (2007)
5. Dupuis, H.: Biodynamic behavior of the trunk and the abdomen during whole-body vibration. Acta Anaesthesiol. Scand. **33**, 34–38 (1989)
6. Paddan, G.S., Griffin, M.J.: The transmission of translational seat vibration to the head—II. Horizontal seat vibration. J. Biomech. **21**, 199–206 (1988)
7. Mirakhorlo, M., Kluft, N., Shyrokau, B., Happee, R.: Effects of seat back height and posture on 3D vibration transmission to pelvis, trunk and head. Int. J. Ind. Ergon. **91**, 103327 (2022). https://doi.org/10.1016/j.ergon.2022.103327
8. Sharma, R.C., Sharma, S., Sharma, S.K., Sharma, N., Singh, G.: Analysis of bio-dynamic model of seated human subject and optimization of the passenger ride comfort for three-wheel vehicle using random search technique. J. Multi-Body Dyn. **235**, 106–121 (2021). https://doi.org/10.1177/1464419320983711
9. Muksian, R., Nash, C.D.: A model for the response of seated humans to sinusoidal displacements of the seat. J. Biomech. **7**, 209–215 (1974)
10. Wei, L., Griffin, M.J.: Mathematical models for the apparent mass of the seated human body exposed to vertical vibration. J. Sound Vib. **212**, 855–874 (1998)
11. Wu, J., Qiu, Y., Sun, C.: Modelling and analysis of coupled vibration of human body in the sagittal and coronal planes exposed to vertical, lateral and roll vibrations and the comparison with modal test. Mech. Syst. Signal Process. **166**, 108439 (2022). https://doi.org/10.1016/j.ymssp.2021.108439
12. Kim, T.-H., Kim, Y.-T., Yoon, Y.-S.: Development of a biomechanical model of the human body in a sitting posture with vibration transmissibility in the vertical direction. Int. J. Ind. Ergon. **35**, 817–829 (2005)
13. Cho, Y., Yoon, Y.-S.: Biomechanical model of human on seat with backrest for evaluating ride quality. Int. J. Ind. Ergon. **27**, 331–345 (2001)
14. Harant, M., Näf, M.B., Mombaur, K.: Multibody dynamics and optimal control for optimizing spinal exoskeleton design and support. Multibody Syst. Dyn. **57**, 389–411 (2023). https://doi.org/10.1007/s11044-023-09877-w
15. Almeida, J., Fraga, F., Silva, M., Silva-Carvalho, L.: Feedback control of the head-neck complex for nonimpact scenarios using multibody dynamics. Multibody Syst. Dyn. **21**, 395–416 (2009). https://doi.org/10.1007/s11044-009-9148-4
16. Kim, E., Fard, M., Kato, K.: A seated human model for predicting the coupled human-seat transmissibility exposed to fore-aft whole-body vibration. Appl. Ergon. **84**, 102929 (2020)
17. Putra, I.P.A., Thomson, R.: Analysis of control strategies for VIVA OpenHBM with active reflexive neck muscles. Biomech. Model. Mechanobiol. (2022). https://doi.org/10.1007/s10237-022-01616-y

18. Putra, I.P.A., Iraeus, J., Sato, F., Svensson, M.Y., Linder, A., Thomson, R.: Optimization of female head-neck model with active reflexive cervical muscles in low severity rear impact collisions. Ann. Biomed. Eng. **49**, 115–128 (2021). https://doi.org/10.1007/s10439-020-02512-1
19. Putra, I.P.A., Iraeus, J., Thomson, R., Svensson, M.Y., Linder, A., Sato, F.: Comparison of control strategies for the cervical muscles of an average female head-neck finite element model. Traffic Inj. Prev. **20**, S116–S122 (2019). https://doi.org/10.1080/15389588.2019.1670818
20. Osth, J., Brolin, K., Brase, D.: A human body model with active muscles for simulation of pretensioned restraints in autonomous braking interventions. Traffic Inj. Prev. **16**, 304–313 (2015). https://doi.org/10.1080/15389588.2014.931949
21. Meyer, F., Bourdet, V., Willinger, R., Legall, F., Deck, C.: Finite element modelling of the human head-neck: modal analysis and validation in the frequency domain. Int. J. Crashworthiness **9**, 535–545 (2004). https://doi.org/10.1533/ijcr.2004.0309
22. Nie, B., Kim, T., Wang, Y., Bollapragada, V., Daniel, T., Crandall, J.R.: Comparison of two scaling approaches for the development of biomechanical multi-body human models. Multibody Syst. Dyn. **38**, 297–316 (2016). https://doi.org/10.1007/s11044-016-9502-2
23. Tass, B.V.: MADYMO Reference Manual. TNO Automotive (2010)
24. Tass, B.V.: MADYMO Model manual. TNO Automotive (2019)
25. Happee, R., Morsink, P., Wismans, J.: Mathematical human body modelling for impact loading (1999) https://doi.org/10.4271/1999-01-1909. SAE Technical Papers
26. Meijer, R., Broos, J., Elrofai, H., De Bruijn, E., Forbes, P., Happee, R.: Modelling of bracing in a multi-body active human model. In: 2013 IRCOBI Conference Proceedings - International Research Council on the Biomechanics of Injury (2013)
27. Happee, R., Hoofman, M., Van Den Kroonenberg, A.J., Morsink, P., Wismans, J.: A mathematical human body model for frontal and rearward seated automotive impact loading (1998) https://doi.org/10.4271/983150. SAE Technical Papers
28. Ambrosio, J., Carvalho, M., Milho, J., Escalante, S., Martin, R.: A validated railway vehicle interior layout with multibody dummies and finite element seats models for crash analysis. Multibody Syst. Dyn. **54**, 179–212 (2022)
29. Rattanagraikanakorn, B., Gransden, D.I., Schuurman, M., De Wagter, C., Happee, R., Sharpanskykh, A., Blom, H.A.P.: Multibody system modelling of unmanned aircraft system collisions with the human head. Int. J. Crashworthiness **25** (2020). https://doi.org/10.1080/13588265.2019.1633818
30. Happee, R., Loczi, J.: Human seat interaction simulation using RAMSIS and the dynamic simulation program MADYMO (1999) https://doi.org/10.4271/1999-01-3737. SAE Technical Papers
31. Meijer, R., Van Hassel, E., Broos, J., Elrofai, H., Van Rooij, L., Van Hooijdonk, P.: Development of a multi-body human model that predicts active and passive human behaviour. In: 2012 IRCOBI Conference Proceedings - International Research Council on the Biomechanics of Injury, pp. 622–636 (2012)
32. Broos, J., Meijer, R.: Simulation method for whiplash injury prediction using an active human model. In: 2016 IRCOBI Conference Proceedings - International Research Council on the Biomechanics of Injury, pp. 390–408 (2016)
33. Mirakhorlo, M., Kluft, N., Desai, R., Cvetkovic, M., Irmak, T., Shyrokau, B., Happee, R.: Simulating 3D Human Postural Stabilization in Vibration and Dynamic Driving. Appl. Sci.-Basel **12** (2022). https://doi.org/10.3390/app12136657
34. Griffin, M.J., Brett, M.W.: Effects of fore-and-aft, lateral and vertical whole-body vibration on a head-positioning task. Aviat. Space Environ. Med. **68**, 1115–1122 (1997)
35. Paddan, G.S., Griffin, M.J.: Transmission of roll and pitch seat vibration to the head. Ergonomics **37**, 1513–1531 (1994)
36. Maciejewski, I., Błażejewski, A., Pecolt, S., Królikowski, T.: Multi-body model simulating biodynamic response of the seated human under whole-body vibration. Proc. Comput. Sci. **207**, 227–234 (2022)
37. Desai, R., Cvetković, M., Wu, J., Papaioannou, G., Happee, R.: Computationally efficient human body modelling for real time motion comfort assessment. In: Scataglini, S., Harih, G., Saeys, W., Truijen, S. (eds.) Advances in Digital Human Modeling, pp. 285–295. Springer, Switzerland (2023)
38. Östh, J., Eliasson, E., Happee, R., Brolin, K.: A method to model anticipatory postural control in driver braking events. Gait Posture **40** (2014). https://doi.org/10.1016/j.gaitpost.2014.07.021
39. Desai, R., Cvetković, M., Wu, J., Papaioannou, G., Happee, R.: Computationally efficient human body modelling for real time motion comfort assessment. In: Scataglini, S., Harih, G., Saeys, W., Truijen, S. (eds.) Advances in Digital Human Modeling, pp. 285–295. Springer, Switzerland (2023)
40. Happee, R., de Bruijn, E., Forbes, P.A., van der Helm, F.C.T.: Dynamic head-neck stabilization and modulation with perturbation bandwidth investigated using a multisegment neuromuscular model. J. Biomech. **58** (2017). https://doi.org/10.1016/j.jbiomech.2017.05.005
41. Happee, R., Kotian, V., De Winkel, K.N.: Neck stabilization through sensory integration of vestibular and visual motion cues. Front. Neurol. **14** (2023). https://doi.org/10.3389/fneur.2023.1266345

42. Kitazaki, S., Griffin, M.J.: A modal analysis of whole-body vertical vibration, using a finite element model of the human body. J. Sound Vib. **200**, 83–103 (1997)
43. Yoshimura, T., Nakai, K., Tamaoki, G.: Multi-body dynamics modelling of seated human body under exposure to whole-body vibration. Ind. Health **43**, 441–447 (2005)
44. Matsumoto, Y., Griffin, M.J.: Non-linear characteristics in the dynamic responses of seated subjects exposed to vertical whole-body vibration. J. Biomech. Eng. **124**, 527–532 (2002)
45. Seidl, A.: RAMSIS - a new CAD-tool for ergonomic analysis of vehicles developed for the German automotive industry (1997) https://doi.org/10.4271/970088. SAE Technical Papers
46. Vogt, C., Mergl, C., Bubb, H.: Interior layout design of passenger vehicles with RAMSIS. Hum. Factors Ergon. Manuf. **15**, 197–212 (2005). https://doi.org/10.1002/hfm.20022
47. Chaffin, D.B.: Human motion simulation for vehicle and workplace design. Hum. Factors Ergon. Manuf. **17**, 475–484 (2007). https://doi.org/10.1002/hfm.20087
48. Katzourakis, D.I., Abbink, D.A., Velenis, E., Holweg, E., Happee, R.: Driver's arms' time-variant neuromuscular admittance during real car test-track driving. IEEE Trans. Instrum. Meas. **63**, 221–230 (2013)
49. Happee, R., de Vlugt, E., van Vliet, B.: Nonlinear 2D arm dynamics in response to continuous and pulse-shaped force perturbations. Exp. Brain Res. **233**, 39–52 (2015)
50. Winter, D.A.: Biomechanics and Motor Control of Human Movement. Wiley, New York (2009)
51. Lugrís, U., Pérez-Soto, M., Michaud, F., Cuadrado, J.: Human motion capture, reconstruction, and musculoskeletal analysis in real time. Multibody Syst. Dyn. (2023). https://doi.org/10.1007/s11044-023-09938-0
52. de Bruijn, E., Van der Helm, F.C.T., Happee, R.: Analysis of isometric cervical strength with a nonlinear musculoskeletal model with 48 degrees of freedom. Multibody Syst. Dyn. **36**, 339–362 (2016)
53. Panjabi, M.M., Crisco, J.J., Vasavada, A., Oda, T., Cholewicki, J., Nibu, K., Shin, E.: Mechanical properties of the human cervical spine as shown by three-dimensional load-displacement curves. Spine **26**, 2692–2700 (2001). https://doi.org/10.1097/00007632-200112150-00012
54. Van Drunen, P., Koumans, Y., van der Helm, F.C.T., Van Dieën, J.H., Happee, R.: Modulation of intrinsic and reflexive contributions to low-back stabilization due to vision, task instruction, and perturbation bandwidth. Exp. Brain Res. **233**, 735–749 (2015)
55. Happee, R., de Bruijn, E., Forbes, P.A., van der Helm, F.C.T.: Dynamic head-neck stabilization and modulation with perturbation bandwidth investigated using a multisegment neuromuscular model. J. Biomech. **58**, 203–211 (2017)
56. Happee, R., de Vlugt, E., Schouten, A.C.: Posture maintenance of the human upper extremity; identification of intrinsic and reflex based contributions. SAE Int. J. Passeng. Cars, Electron. Electr. Syst. **1** (2009)
57. Schouten, A.C., Mugge, W., van der Helm, F.C.: NMClab, a model to assess the contributions of muscle visco-elasticity and afferent feedback to joint dynamics. J. Biomech. **41**, 1659–1667 (2008). https://doi.org/10.1016/j.jbiomech.2008.03.014
58. de Vlugt, E., Schouten, A.C., van der Helm, F.C.: Quantification of intrinsic and reflexive properties during multijoint arm posture. J. Neurosci. Methods **155**, 328–349 (2006). https://doi.org/10.1016/j.jneumeth.2006.01.022
59. van Dieën, J.H., van Drunen, P., Happee, R.: Sensory contributions to stabilization of trunk posture in the sagittal plane. J. Biomech. (2017). https://doi.org/10.1016/j.jbiomech.2017.07.016
60. van Drunen, P., Koumans, Y., van der Helm, F.C.T., van Dieën, J.H., Happee, R.: Modulation of intrinsic and reflexive contributions to low-back stabilization due to vision, task instruction, and perturbation bandwidth. Exp. Brain Res. **233** (2015). https://doi.org/10.1007/s00221-014-4151-2
61. Panjabi, M.M., Crisco, J.J., Vasavada, A., Oda, T., Cholewicki, J., Nibu, K., Shin, E.: Mechanical properties of the human cervical spine as shown by three-dimensional load–displacement curves. Spine **26**, 2692–2700 (2001)
62. Camacho, D.L., Nightingale, R.W., Robinette, J.J., Vanguri, S.K., Coates, D.J., Myers, B.S.: Experimental flexibility measurements for the development of a computational head-neck model validated for near-vertex head impact. SAE transactions, 3989–4002 (1997)
63. Henriques, D., Martins, A.P., Carvalho, M.S.: Efficient 2D neck model for simulation of the whiplash injury mechanism. Bioengineering **11**, 129 (2024)
64. Transfer function estimate - Matlab tfestimate - MathWorks Benelux. https://nl.mathworks.com/help/signal/ref/tfestimate.html
65. Desai, R., Cvetković, M., Papaioannou, G., Happee, R.: Modelling human seat contact interaction for vibration comfort. Comfort Congress. (2023)
66. Mandapuram, S.C., Rakheja, S., Ma, S., Demont, R.G., Boileau, P.-E.: Influence of back support conditions on the apparent mass of seated occupants under horizontal vibration. Ind. Health **43**, 421–435 (2005)
67. Wegner, M., Martic, R., Franz, M., Vink, P.: A system to measure seat-human interaction parameters which might be comfort relevant. Appl. Ergon. **84** (2020). https://doi.org/10.1016/j.apergo.2019.103008